Reverse engineering the control law for schooling in zebrafish using virtual reality

Liang Li[1,2,3*], Máté Nagy[1,2,3,4,5*], Guy Amichay[1,2,3,6,7], Ruiheng Wu[2,8,1], Wei Wang[9], Oliver Deussen[2,8], Daniela Rus[10], and Iain D. Couzin[1,2,3*]

[1] Department of Collective Behaviour
Max Planck Institute of Animal Behavior, 78464 Konstanz, Germany
[2] Centre for the Advanced Study of Collective Behaviour
University of Konstanz, 78464 Konstanz, Germany
[3] Department of Biology
University of Konstanz, 78464 Konstanz, Germany
[4] MTA-ELTE "Lendület" Collective Behaviour Research Group
Hungarian Academy of Sciences, 1117 Budapest, Hungary
[5] Department of Biological Physics
Eötvös Loránd University, 1117 Budapest, Hungary
[6] Department of Engineering Sciences and Applied Mathematics
Northwestern University, Evanston, IL, USA
[7] Northwestern Institute on Complex Systems
Northwestern University, Chicago, Illinois, USA
[8] Department of Computer and Information Science
University of Konstanz, 78464, Konstanz, Germany
[9] Department of Mechanical Engineering
University of Wisconsin–Madison, Madison, WI 53706, USA
[10] Computer Science and Artificial Intelligence Lab (CSAIL)
Massachusetts Institute of Technology, Cambridge, MA, USA

*To whom correspondence should be addressed;
E-mail: lli@ab.mpg.de, mate.nagy@ttk.elte.hu, and icouzin@ab.mpg.de.

Revealing the evolved mechanisms that give rise to collective behavior is a central objective in the study of cellular and organismal systems. Additionally, understanding the algorithmic basis of social interactions in a causal and quantitative way offers an important foundation for subsequently quantifying social deficits. Here, with Virtual Reality (VR) technology, we employ virtual robot fish to reverse-engineer the sensory-motor control of social response during schooling in a vertebrate model: juvenile zebrafish (*Danio rerio*). In addition to providing a highly-controlled means to understand how zebrafish translate visual input to movement decisions, networking our systems allows real fish to swim and interact together in the same virtual world. Together, this allows us to directly test models of social interactions in situ. A key feature of social response is shown to be single- and multi-target-oriented pursuit. This is based on an egocentric representation of the positional information of conspecifics, and is highly robust to incomplete sensory input. We demonstrate, including with a Turing test and a scalability test for pursuit behavior, that all key features of this behavior are accounted for by individuals following a simple experimentally-derived proportional derivative control law, which we term 'BioPD'. Since target pursuit is key to effective control of autonomous vehicles, we evaluate—as a proof of principle—the potential utility of this simple evolved control law for human-engineered systems. In doing so, we find close-to-optimal pursuit performance in autonomous vehicle (terrestrial, airborne, and watercraft) pursuit, while requiring limited system-specific tuning or optimization.

Summary

Reverse engineering the control law employed by schooling fish provides an effective and robust algorithm for robotic pursuit

Reverse engineering evolved control laws

INTRODUCTION

Collective behavior arises from positive and/or negative local feedback loops, which enable repeated local interactions to scale up into highly robust coordinated activities without the need for regulation by global supervision or via a pre-established template (*1, 2*). Due to their ubiquity and importance across scales of biological organization, the mechanisms that give rise to coordinated motion among cells (*3*) and organisms such as swarming insects (*4, 5*), schooling fish (*6–8*), flocking birds (*9, 10*), and humans in crowds (*11, 12*), have been of particular interest across multiple disciplines. In addition to providing new insights into biology, an understanding of the evolved strategies animals employ to coordinate collective behavior can offer new opportunities for the development of engineered solutions (*13*), such as for the coordination of autonomous vehicles (*14, 15*).

To date, however, it has been extremely difficult to infer the nature and causal structure of biological interactions that give rise to collective behavior using conventional experimental approaches (*16–18*). Consequently, the sensory-motor feedback mechanisms that have evolved to regulate collective behavior are often poorly understood (*19*), with our inability to identify, or test among, alternative hypotheses being a major bottleneck. Recent advances in immersive volumetric virtual reality (VR) technology (*20–22*) provide a new means to control, and thus interrogate, the causal structure of social relationships among individuals. In addition, they allow the direct testing of experimentally-derived hypothetical models of social interactions in situ, by

allowing reciprocal coupling between real organisms and virtual robot fish as counterparts (*23*). Thus, analogous to how the 'dynamic patch clamp' method has revolutionized neuroscience, creating a realtime interface between living cells and experimentally-derived models (*24*), virtual reality opens up a 'dynamic social clamp' approach (*23*) to the study of animal behaviour.

In this study, we applied a virtual reality platform (*20*) to control virtual conspecifics which can interact with real fish, enabling us to reverse-engineer the fundamental sensory-motor control mechanisms governing leader-follower dynamics under various conditions (Fig. 1A, fig. S1, and Movie 1). We discovered that a simple, yet powerful, proportional derivative-like controller, which we term "BioPD", effectively captures the social pursuit behavior of fish (Fig. 1B-D). To validate the model, we explored its assumptions, assessed its predictive capabilities, and conducted a Turing test with real fish—all of which confirmed the model's effectiveness (Fig. 1D-F). Finally, we appiled BioPD to different robotic systems, tested the scalability of the model in large-scale fish schools across different species, and integrated it into various robotic platforms for diverse group sizes and pursuit tasks (Fig. 1G-I). Our findings highlight the potential of robotic platforms, such as virtual reality, as valuable tools for understanding collective behavior while simultaneously, in return, inspiring advancements in robotic control design.

RESULTS

Development and validation of the immersive virtual reality system

We applied an immersive virtual reality for fish (*20*) to investigate the sensory-motor control employed in regulating schooling behaviour in a model vertebrate, the juvenile zebrafish (*Danio rerio*) (1$\pm$0.1 cm in length, 24-26 days post fertilisation, Fig. 1 and Movie 2). At this age zebrafish predominantly employ vision to coordinate response to conspecifics when schooling (the lateral line being dominated by self-generated motion due to viscous adhesion forming a boundary layer around such small fish (*25*)).

Since leading others is known to be driven by different internal processes, such as indifference to others (*26*) and motion towards external goals (*27*), as a valuable starting point—and due to its general importance—we focus here only on socially-mediated interactions. In addition to uncovering a key algorithm employed in regulating schooling behavior (Fig. 1B-F, H, Supplementary Methods, fig. S1, and Table S1), we demonstrated its application to motion control in engineered systems (Fig. 1G, I).

Since our immersive virtual reality, for freely swimming animals, relies on correct volumetric rendering from the perspective of a single individual (via the anamorphic illusion), it is not possible to put more than one individual in each VR arena. We can, however, connect systems (*28*) such that individuals can see, and thus interact with, a realtime 'holographic' projection of the other (Fig. 1C shows this principle for a pair of individuals), which we term "the Matrix" (Movie 2). We found that, as in the real world (figs. S2A-D, S3A-D, and S4A-C), individuals in "the Matrix" (figs. S2E-H, S3E-H, and S4B-D) interact only when they occupy the same $x - y$ plane, with even small movements out of that plane (in the z dimension), either towards the surface, or to deeper water, being associated with rapid decoupling of social interactions (fig. S5). The structure, and strength, of the interactions within this plane (as quantified by decomposing motion to lateral speed v_x, which is perpendicular to the leader's head direction, and forward speed v_y, which is along the leader's head direction (Fig. 2A)), is found to be near-identical when they interact within the physical world (fig. S4A-C) as when they interact in the same holographic world (fig. S4B, D and fig. S6, Kolmogorov–Smirnov test, p=0.26 for v_x, p=0.9 for v_y). This suggests our VR system is ideal for dissecting sensory-motor feedback control.

Reverse engineering the sensory-motor feedback control

To do so, we first conducted open-loop experiments, which allow us to control the causal flow of information from a leading (virtual) fish to a following (real) fish (Fig. 2B). Our platform also enables us to isolate and analyze how social responses are influenced by both spatial factors and average swim speed. Here we evaluated average swim speed across its natural range, while also accounting for its inherently bursty nature—characterized by rapid tail undulations followed by a friction-dominated glide (Fig. 2C and fig. S7).

Fish tend to follow/pursue the virtual leader at a relatively stable distance, with this distance increasing approximately linearly as a function of the leader's speed (Fig. 2D-J and fig. S8), but with different "times to collision" (with respect to the current position of the leader, if the leader were to suddenly stop; fig. S9). The decomposed lateral (v_x) and forward (v_y) components of the follower's speed, as a function of the spatial position of the follower relative to a leader positioned at x= 0, y= 0, are shown in Fig. 2E, F, respectively. As shown in Fig. 2G, the average lateral speed increases as a function of lateral distance (x-axis) up to a specific distance, r_x = 0.07m (determined by finding the maximum lateral speeds following a bootstrapping procedure; see Supplementary Methods for details), indicated by the dotted line, after which it starts to decrease. Lateral speed is minimally influenced by swim speed (as seen by the similarity of panels in Fig. 2E and the average plots in Fig. 2G). The magnitude of the forward speed component as a function of the front-back distance, shown in Fig. 2H, also increases up to a similar distance, r_y = 0.07m (see Supplementary Methods for details), but, unlike lateral speed, it increases in absolute magnitude as a function of average swim speed of the leader.

According to the above properties (speed control being proportional to the distance lag and to the average swimming speed of the leader, plus a lateral point of speed reduction at a specific distance), and following reverse engineering methods in biological studies (*29–35*), we

proposed a parsimonious bio-inspired Proportional-Derivative (PD) controller, 'BioPD':

$$\begin{cases} x_e &= x_F - x_L \\ v_x &= -(K_p x_e + K_d \dot{x}_e) e^{-\frac{x_e^2}{2r_x^2}} \\ y_e &= y_F - y_L \\ v_y &= -(K_p y_e + K_d \dot{y}_e) e^{-\frac{y_e^2}{2r_y^2}} \end{cases} \quad (1)$$

where x_F, y_F (and respectively, x_L, y_L) are the positions of the follower (leader) in a global coordinate system resolved in the x- and y- axes according to the leader (Fig. 2A). r_x and r_y, describe the critical distances at which the strength of social interactions is largest (Supplementary Methods). K_d and K_p are the derivative gain and proportional gain parameters, respectively, which are the two main parameters in the model. We first determined the derivative parameter, based on the relationship between the average forward swimming speed of real and virtual fish (see Supplementary Methods for details), finding K_d =0.58 (Fig. 2I). The proportional parameter K_p is estimated based on the stable distance lag under different average swimming speeds of the leader, which for our zebrafish is found to be a constant with value K_p =2.3 (Fig. 2J).

Despite its simplicity, we found that the BioPD model can account for all of the main features observed in our experiments, including the stable swim speed of the follower, which is matched to that of the leader (fig. S10A, B), a similar spatial probability density with respect to the leader and similar lateral and forward swimming speeds as a function of x_e and y_e (fig. S10C-F). This indicates that a simple PD-like controller, with identical parameters, can effectively regulate schooling fish, irrespective of the average swim speed of the leader.

Validation of the assumptions of the BioPD model

Speed input in a PD controller can be either the instantaneous speed or the average speed over some period of time, as perceived directly through the fish's vision. Therefore, we further used our virtual robotic conspecifics to evaluate, directly, which features of the speed of conspecifics are employed in regulating social response. Previously, it has been suggested that the motion

characteristics associated with burst-and-glide locomotion of juvenile zebrafish may provide an important social cue (*36*). However, using virtual fish swimming with burst-and-glide as the control (Fig. 3A(ii)) and constant-speed swimming at the same average speed as the treatment (Fig. 3A(ii) and Movie 2), we observed that the following distance lag (Fig. 3A(iii) vs (iv)), lateral speed (Fig. 3A(v) vs (vi)), and forward speed (Fig. 3A(vii) vs (viii)) are same. This indicates that zebrafish respond similarly to continuous motion as they do to biological (bursty) motion (see fig. S11 for a detailed comparison).

This suggests that fine-scale instantaneous speed is not employed in the regulation of schooling. To evaluate this further, we investigated how the temporal resolution of visual input influences social response. By systematically changing the temporal update frequency, such that the virtual fish is always visible, but that its position is only updated at a certain rate (for instance, if the frequency is 10 Hz, the position of the virtual fish will be updated 10 times per second, the frames between which it does not change position, fig. S12 and Movie 2), we found that only if the update rate falls below $\sim$5Hz does the distance lag increase (Fig. 3B(iii)-(iv)), indicating a diminishing of the effectiveness of the social response below this frequency. (Fig. 3B). This indicates that zebrafish integrate information over approximately 0.2s, a timescale close to the typical period of their burst-and-glide gait (fig. S7), which may imply the use of spatial working memory (*37*) and is captured in the model by averaging speed with a similar time window.

To establish how robust the schooling response is in the face of incomplete information, we decoupled speed and position by manipulating the visibility of the virtual fish. As may be expected of animals that need to deal with regular occlusions of others, such as by vegetation, or in patches of high turbidity, they do not respond to the sudden disappearance, or appearance, of a conspecific (Fig. 3C, D, figs. S13, S14, and Movie 2). By adjusting both the duration of the windows of time during which information is available (figs. S12, S13), as well as whether the perceived speed in these windows is (Fig. 3C(ii)), or is not (Fig. 3D(ii)), congruent with the

displacement (such as the average speed) between these windows (fig. S14), we observed no difference in distance lag, lateral speed, or forward speed when the perceived speed matches the invisible case (Fig. 3C(iii)-(viii)). However, there is a substantial difference in the non-matching case (Fig. 3(iii)-(viii)). This suggests that the algorithm employed by zebrafish employs positional information as the input for speed control, and not estimates of instantaneous speed (Fig. 3C, D and figs. S13, S14).

Predictive power of BioPD

With the core assumptions of BioPD validated, we then asked whether it can account for further dynamical features of natural schooling. In order to establish the above control law, we employed virtual robot fish as conspecifics that move in a constant direction and at a constant average swim speed. In reality, however, fish dynamically modulate both properties. By presenting exactly the same trajectories, obtained from real fish leaders, both to real fish and to agents employing BioPD (Fig. 4A, B), we compared directly the response of real followers with agents employing BioPD. We found that BioPD provides robust and effective response to the dynamic changes in speed and direction exhibited in the natural system, and results in highly-comparable pursuit behavior to that exhibited by real fish (Fig. 4E, F).

Our VR systems allow us to take an even further step in establishing sensory-motor control; we could also ask whether leaders react differently to real followers versus followers employing BioPD. This can be thought of as a Turing test for the leader: is an agent employing BioPD sufficiently convincing to allow natural bi-directional interactions? To do so, we now allow two real fish, A and B, to interact in "the Matrix", but each time fish A becomes a leader (such as when it occupies a frontal position), we can immediately replace the natural control of B with our BioPD control, and vice versa (Fig. 4C, D, fig. S15, and Movie 2). Thus we compared what we predict fish will do to what they actually do, for every pursuit event. We found that

187 despite its simplicity, BioPD facilitates the maintenance of qualitatively similar, and effective,
188 reciprocal social relationships among hybrid simulated-real individuals (Fig. 4G, H).

189 Having established the response to a single conspecific, we then asked whether BioPD can
190 also predict the response of real fish to two virtual conspecifics (*38*). To do so, we considered its
191 response to two leaders swimming side-by-side at a range of inter-individual lateral distances
192 and swim speeds (Fig. 4I, J and Movie 2). We simply applied the BioPD controller for an agent
193 receiving sensory input from the two leaders, but taking into account the linear perspective in
194 the fish eye (see Supplementary Methods for details). We found that BioPD accounts, quan-
195 titatively, for a key experimental finding, as the blue points predicted by the model match the
196 high-density regions of real fish behavior data in Fig. 4K and L; that real fish will both change
197 their distance lag (Fig. 4K) and will suddenly switch from adopting a position in-between the
198 targets (here, the leaders) to deciding among them (swimming predominantly with one of the
199 virtual fish) as a function of increasing the lateral distance, l, between the virtual leaders (Fig.
200 4L and fig. S16). Furthermore, it also accounts for the observed increase in the critical distance
201 (l_c) at which this transition occurs as a function of increasing swim speed (Fig. 4L and figs.
202 S17-S19).

203 Scalability of BioPD

204 To investigate the scalability and generalizability of our BioPD and its potential in elucidating
205 collective behavior in large groups, we analyzed the social response of followers in schools of
206 juvenile zebrafish (*Danio rerio*, N=20) tracked with custom code (*39*), juvenile golden shiners
207 (*Notemigonus crysoleucas*, N=10, 30, 70, 150, data from previous publication (*40*)), and ju-
208 venile sunbleak (*Leucaspius delineatus*, N=512, 1024) tracked with custom code (*39*). Across
209 all three species, we observed pervasive leader-following behavior, even in larger group sizes.
210 Analogous to the two-fish system, the distance lag correlates with the leading fish's average

swimming velocity. The follower's turning and forward speeds align with characteristics previously observed in our virtual reality system (Fig. 5A-C, fig. S20). Such findings suggest that the BioPD derived from smaller groups can be extrapolated to larger collectives.

Robotic applications of BioPD

Reverse engineering natural control laws—which have been subject to evolution by natural selection for millennia—could, in principle, provide simpler and/or more robust solutions for human-engineered problems (*13*). The effective pursuit of mobile targets, along with the maintenance of appropriate spacing with respect to a target (which can include interception, or pursuit while also avoiding collisions, for example), is a central challenge in the effective control of autonomous vehicles, such as self-driving cars and guided aircraft and spacecraft. Human-made controllers, such as the widely-employed model predictive controller (MPC) (*41*), have been shown to be optimal for certain tasks, but typically are computationally expensive due to the fact MPCs are solving an optimization problem over a predicted horizon (predicting future system behavior over a defined time frame) at each control step. Moreover, MPCs need to be individually optimized—a very time-consuming process—for each specific application (since they depend on an accurate underlying model of the dynamical systems in which they are to be embedded). Natural systems, by contrast, are under the section to evolve highly robust and cheap strategies that approximate optimal solutions under a wide range of conditions. Seldom, however, are such evolved solutions evaluated in situ in real physical systems.

To gain insight into such potential application domains, we implemented, and compared the pursuit performance of a state-of-the-art optimal MPC controller (see Supplementary Methods for details) and BioPD in three very different robotic platforms; terrestrial vehicles, airborne drones (*42*), and watercraft (Fig. 1H), the task being to follow a virtual leader on a predefined sine-shaped trajectory (Fig. 4M, Movie 3). Furthermore, unlike the MPC controller, which

required a complex and time-consuming optimisation procedure for each robotic system, we employed BioPD with exactly the same parameters as estimated from zebrafish in all scenarios. We found that with suboptimal control parameters extracted from biological system (Figs. S21, S22), and despite its simplicity, BioPD exhibits highly robust and effective performance, providing very close to optimal control energy (*43*) in the vehicle, drone, and roboboat control tasks (Fig. 4N and figs. S23-S25). To further assess the scalability of BioPD (Movie 3), we used the BioPD to direct 14 robots in a sequential circular motion (Fig. 5D), three robots in tracing an intricate path of the letters associated with our research center, "CASCB" (Fig. 5E), and 14 robots in emulating real fish trajectories (18x larger scale) at both constant (Fig. 5F) and varying speeds (Fig. 5G). The corresponding deviation of each robot's trajectory to the desired path, distance lag between successive pairs of robots in the sequence, moving speeds, and control energy are illustrated in Fig. 5H-K and figs. S26-S29.

DISCUSSION

In this study, we constructed a virtual robotic 'conspecific' for juvenile zebrafish and utilized it to reverse engineer the algorithm employed to regulate social response. After confirming that real fish accept the virtual robotic fish as a 'conspecific' at the behavioral level, we demonstrated that a simple PD-like controller ('BioPD') can account for the social response exhibited towards it by real fish (Fig. 2). Taking advantage of the virtual robot platform, we systematically checked the assumptions of the model (Fig. 3), verified the effectiveness of the model (Fig. 4A-H), tested its power of prediction (Fig. 4I-L), explored its potential applications (Fig. 4M-N), and demonstrated its scalability (Fig. 5). These tests illustrate that the platform is a powerful tool for quantitatively and causally exploring hidden internal controls, offering capabilities that have been largely inaccessible in previous systems.

By controlling the visibility of the virtual robot to decouple position and speed perception

(something not possible in traditional biological experiments or even with those physical replicas (*28*)), we found that fish primarily rely on position perception rather than instantaneous speed perception (Fig. 3). Additionally, the input for derivative control on long-term average speed is derived from positional information (fig. S13). This mechanism is similar to a low-pass filter and could facilitate noise reduction in the velocity control. However, it remains unclear how fish obtain neighbor's positional information from their visual scene, and this will be the focus of our future studies. Despite being derived from the response to a single leader we found that BioPD can also account for the fish behavior when presented with two leaders; notably an abrupt transition (bifurcation) from averaging to deciding to follow one, or the other, of the potential leaders as a function of the distance between them (Fig. 4I-L). This finding is consistent with our previous work on geometric principles that emerge from individual decision-making (*38*), where the linear distortion of perspective provides a comparable 'non-Euclidean' distortion of space (*38, 44*).

Our study suggests that fish may have evolved a sensorimotor control like BioPD as it provides a cognitively-minimal, yet highly-effective means to regulate schooling. Compared to traditional PD-like controllers in engineering systems (*45, 46*), our controller differs in two key ways: First, it introduces a biologically meaningful cut-off in the interaction, embedded through a non-linear first-order Gaussian function (Fig. 2G, H), and second, it has been validated in biological systems through assumption verification (Fig. 3A-D), predictive power testing (Fig. 4I-L), and even an embodied Turing test (Fig. 4A-H). This uniquely bridges engineering and biological systems. Unlike traditional PD controllers in biological systems that either explore PD functions within the system (*33, 47*) or aim to find the best controllers to fit biological data (*30, 48, 49*), our approach focuses on reverse-engineering the complete dynamics of pursuit behavior. We offer a detailed controller along with measured parameters, rather than merely fitting the data.

The reason BioPD generalizes well to the three robotic platforms may be the same reason it has evolved; because the control is based on a kinematic model, without involving specific dynamics, it is highly generalised. Therefore, there is room for optimization for each robot based on the dynamic models of their respective systems (Fig. 4N and figs. S21, S22), which will be our future focus. In the future, we will also explore in further detail the limitations and potential applications of this controller. In our preliminary analysis of scalability, we found that fish adopt the same interaction rule in the pursuit behavior as when in large groups (Fig. 5). Overall, our work suggests that reverse-engineering the control law in schooling fish using virtual 'conspecifics' offers a complementary approach to traditional methods in both biology and engineering. It is valuable not only for systematically exploring potential internal sensory-motor controls in biological systems but also for designing controllers that are efficient and robust, requiring minimal sensing and computational resources.

MATERIALS AND METHODS

Methodological overview

We developed and utilized a virtual reality platform to reverse engineer the sensory-motor control algorithm for schooling behavior (fig. S1). To confirm its effectiveness, we compared the speed control of a real fish to another real fish in a traditional platform with that to a virtual fish in our system. Subsequently, we conducted open-loop experiments in the virtual environment with a single virtual fish, where we controlled the leader's swimming properties, such as average speed, patterns, and visibility. By doing so, we developed a biologically inspired proportional derivative control model for the following behavior and verified its assumptions. Furthermore, we estimated the model through various methods, including simulations, experiments in the virtual reality system, experiments with two virtual leaders, and tests with three types of robots (terrestrial, airborne, and watercraft).

The virtual reality platform

The test arena is bowl-shaped, holding 4.5 liters of water, with a depth in the centre of 9.1 cm and a diameter of 33.8 cm. The bowl is made from a material that is opaque to visible light but transparent to infrared light, allowing us to illuminate it from below with infrared light (wavelength 850 nm) for tracking purposes. Positioned above the bowl are four Basler acA640 cameras, capturing images at 100 fps in real time. The 3D position of the real fish is reconstructed from its detected position in each view using blob detection. With these reconstructed 3D positions, we track the fish's movements based on an Extended Kalman Filter and the nearest neighbor standard filter for data association. An LED (light-emitting diode) DLP (digital light processing) projector (Optoma ML500) illuminates the entire surface of the bowl to allow us to present the virtual scene in the visible light spectrum. To ensure accurate projection, the projected image is mapped onto the 3D curvature of the bowl using a calibration model of the display geometry. A grid is rendered during calibration, mapping each pixel to its corresponding geometric coordinates. The anamorphic illusion is applied to render the image as 3D scene from the correct perspective of the real fish. A virtual fish, modeled in Blender (Blender Foundation) based on juvenile zebrafish (26 dpf, 1cm), is rendered within the system to interact with freely swimming real fish (24-27 dpf, 1±0.1 cm) in 3D (*20, 50*). In "the Matrix setup", similar to (*28*), the real fish's position and orientation are tracked on one machine and transferred in real time to another machine via a socket connection, allowing for seamless bidirectional communication between the two systems. For further details, please refer to our previous work (*20, 50*).

Virtual reality experiments

We conducted experiments with zebrafish (*Danio rerio*) of age 24 to 26 days postfertilization raised in a room at 28 degrees on a 16-h light, 8-h dark cycle. The variation in age was to allow us to always use fish of a similar body length (1$\pm$0.1 cm). 498 zebrafish were used (See

table S1). Experiments were conducted in a fish virtual reality setup procured from Loopbio GmbH (refer to ref. (*20*) for details). After a fish was introduced into the arena (a bowl-shaped container with a diameter of 34 cm and a depth of 9 cm at the water level), we allowed the fish to acclimate to the environment for 20 minutes. This was followed by a 10-min control, during which the fish was presented with a single virtual conspecific (1 cm in body length) swimming in a circle with a diameter of 16 cm. After this, the real fish was exposed to the virtual fish, initialized with various swimming conditions (Supplementary Methods). Each experiment lasted 90 minutes. We analyzed the data using custom Python 3.7 code. All experiments were conducted in accordance with the animal ethics permit approved by Regierungspräsidium Freiburg, G-16/116, G-17/88, and G-17/170.

Simulations

We utilized the BioPD algorithm to simulate the behavior of following a virtual leader in the VR experiment, as well as a real leader in a pair of fish performing leader-follower behavior extracted from real fish data. For following the virtual leader, we set the follower's initial position to a range of -0.05 to 0.05 m on the x-axis and -0.05 to 0 m on the y-axis. We introduced variability by adding white noise to the follower's speed control, with a standard variance of 0.016 for the x-axis and 0.45 times the average speed of the follower for the y-axis. The maximum swimming speed was limited to 0.1 m/s. In contrast, for following a real fish leader, we initialized the geometry position and swimming probabilities of the follower to match the starting point of leader-follower behavior in the pair of real fish swimming in the same arena. The only difference in this model from the previous one is that the leader is extracted from real fish leader data, which dynamically changes both average swimming speeds and directions. No noise was added in the second simulation.

Parameter estimation for the model

The BioPD model has four primary parameters (r_x, r_y, K_p, K_d), which we determined by measuring real fish data collected in the virtual reality experiments. In the following behavior, when the distance between the leader and follower is larger than the threshold distance r_x (r_y), the follower reduces its speed to follow the leader. Therefore, we modeled the turning point of speed as a first-order Gaussian derivative function, with the threshold distance corresponding to the peak of the function. We determined the threshold distance by bootstrapping (Supplementary Methods). Since the follower must be within the distance threshold to catch up with the leader, we simplified the model to a traditional PD controller. By analyzing the PD controller, we found that the average swimming speed of the leader and follower is determined by a first-order linear function, where the slope is determined by K_d only, and the intercept is determined by both K_p and K_d. We obtained these two parameters through a similar bootstrap analysis, and detailed derivations are given in Supplementary Methods.

Robotic experiments

We tested both BioPD and an optimal controller on three different types of robots: the Crazyflie drone (*42*), the SunFounders Robot PiCar-X, Osoyoo Robot Pi Car and a robot boat. To create a virtual leader for the robots to follow, we programmed it to move in a sinusoidal curve. We applied BioPD with the same mathematical model and parameters, which were scaled by the body size of the robots. Additionally, we considered a MPC based on our previous study (*41*). To achieve the best performance with MPC, parameters are optimized for each type of robot. Further details can be found in Supplementary Methods.

Statistical analysis

We applied bootstrap resampling to estimate the variability in the relationships between lateral speed (v_x) and position in x, as well as forward speed (v_y) and position in y. Specifically, we resampled the collected data 100 times and plotted the average trends along with their variability, as shown in Fig. 2G and H. To evaluate the similarity between real fish interactions in the physical world and those in "the Matrix", we computed the root-mean-square deviation (RMSD) of lateral speed (v_x) and forward speed (v_y) as functions of the neighbor's position. Data from 22 real interaction pairs in the physical world were pooled to serve as a reference. We then compared this reference to the RMSD of the remaining 24 real pairs and 24 virtual ("the Matrix") pairs. Kolmogorov–Smirnov tests revealed no significant differences between the real and virtual conditions (lateral speed: $p = 0.26$; forward speed: $p = 0.9$). To further check the similarity among the simulations, the BioPD model, and the Turing test, we applied the Jensen–Shannon Divergence (JSD). The results showed minimal divergence: $\mathrm{JSD} = 0.03$ for forward swimming between simulations and the model (Fig. 4E), $\mathrm{JSD} = 0.0$ for turning speed between simulations and the model (Fig. 4F), $\mathrm{JSD} = 0.08$ for forward swimming between real fish and the model in the Turing test (Fig. 4G), and $\mathrm{JSD} = 0.0$ for turning speed between real fish and the model in the Turing test (Fig. 4H). A standard boxplot—featuring the median, interquartile range (IQR), and potential outliers—was used to illustrate the deviation between the robots' trajectories and the desired path, as shown in Fig. 5H-K.

Data and materials availability

All data necessary to understand and evaluate the conclusions are available in the main text or the Supplementary Materials. Source data and code are available via Dryad (DOI: 10.5061/dryad.np5hqc02k).

References

1. S. Camazine, J.-L. Deneubourg, N. R. Frank, J. Sneyd, G. Theraulaz, E. Bonabeau, *Self-Organization in Biological Systems* (Princeton Univ., Princeton, NJ, 2003).

2. D. J. T. Sumpter, *Collective Animal Behavior* (Princeton Univ., Princeton, NJ, 2010).

3. T. S. Deisboeck, I. D. Couzin, Collective behavior in cancer cell populations. *BioEssays* **31**, 190–197 (2009).

4. J. Buhl, D. J. T. Sumpter, I. D. Couzin, J. J. Hale, E. Despland, E. R. Miller, S. J. Simpson, From disorder to order in marching locusts. *Science* **312**, 1402–1406 (2006).

5. P. Ramdya, P. Lichocki, S. Cruchet, L. Frisch, W. Tse, D. Floreano, R. Benton, Mechanosensory interactions drive collective behaviour in Drosophila. *Nature* **519**, 233–236 (2014).

6. A. J. W. Ward, J. E. Herbert-Read, D. J. T. Sumpter, J. Krause, Fast and accurate decisions through collective vigilance in fish shoals. *Proc. Natl. Acad. Sci. U.S.A.* **108**, 2312–2315 (2011).

7. A. Berdahl, C. J. Torney, C. C. Ioannou, J. J. Faria, I. D. Couzin, Emergent sensing of complex environments by mobile animal groups. *Science* **339**, 574–576 (2013).

8. R. C. Hinz, G. G. de Polavieja, Ontogeny of collective behavior reveals a simple attraction rule. *Proc. Natl. Acad. Sci. U.S.A.* **114**, 2295–2300 (2017).

9. M. Ballerini, N. Cabibbo, R. Candelier, A. Cavagna, E. Cisbani, I. Giardina, V. Lecomte, A. Orlandi, G. Parisi, A. Procaccini, M. Viale, V. Zdravkovic, Interaction ruling animal collective behavior depends on topological rather than metric distance: Evidence from a field study. *Proc. Natl. Acad. Sci. U.S.A.* **105**, 1232–1237 (2008).

10. A. Flack, M. Nagy, W. Fiedler, I. D. Couzin, M. Wikelski, From local collective behavior to global migratory patterns in white storks. *Science* **360**, 911–914 (2018).

11. M. Moussaid, D. Helbing, G. Theraulaz, How simple rules determine pedestrian behavior and crowd disasters. *Proc. Natl. Acad. Sci. U.S.A.* **108**, 6884–6888 (2011).

12. A. C. Gallup, J. J. Hale, D. J. T. Sumpter, S. Garnier, A. Kacelnik, J. R. Krebs, I. D. Couzin, Visual attention and the acquisition of information in human crowds. *Proc. Natl. Acad. Sci. U.S.A.* **109**, 7245–7250 (2012).

13. G.-Z. Yang, J. Bellingham, P. E. Dupont, P. Fischer, L. Floridi, R. Full, N. Jacobstein, V. Kumar, M. McNutt, R. Merrifield, B. J. Nelson, B. Scassellati, M. Taddeo, R. Taylor, M. Veloso, Z. L. Wang, R. Wood, The grand challenges of Science Robotics. *Sci. Robot.* **3**, eaar7650 (2018).

14. J. Werfel, K. Petersen, R. Nagpal, Designing collective behavior in a termite-inspired robot construction team. *Science* **343**, 754–758 (2014).

15. F. Berlinger, M. Gauci, R. Nagpal, Implicit coordination for 3D underwater collective behaviors in a fish-inspired robot swarm. *Sci. Robot.* **6**, eabd8668 (2021).

16. M. Nagy, Z. Akos, D. Biro, T. Vicsek, Hierarchical group dynamics in pigeon flocks. *Nature* **464**, 890–893 (2010).

17. S. Marras, R. S. Batty, P. Domenici, Information transfer and antipredator maneuvers in schooling herring. *Adapt. Behav.* **20**, 44–56 (2012).

18. K. R. Pilkiewicz, B. H. Lemasson, M. A. Rowland, A. Hein, J. Sun, A. Berdahl, M. L. Mayo, J. Moehlis, M. Porfiri, E. Fernández-Juricic, S. Garnier, E. M. Bollt, J. M. Carlson,

M. R. Tarampi, K. L. Macuga, L. Rossi, C. C. Shen, Decoding collective communications using information theory tools. *J. R. Soc. Interface* **17**, 20190563 (2020).

19. A. Laan, R. G. de Sagredo, G. G. de Polavieja, Signatures of optimal control in pairs of schooling zebrafish. *Proc. R. Soc. B* **284**, 20170224 (2017).

20. J. R. Stowers, M. Hofbauer, R. Bastien, J. Griessner, P. Higgins, S. Farooqui, R. M. Fischer, K. Nowikovsky, W. Haubensak, I. D. Couzin, K. Tessmar-Raible, A. D. Straw, Virtual reality for freely moving animals. *Nat. Methods* **14**, 995–1002 (2017).

21. H. Naik, R. Bastien, N. Navab, I. D. Couzin, Animals in virtual environments. *IEEE Trans. Vis. Comput. Graph.* **26**, 2073–2083 (2020).

22. S. Sayin, E. Couzin-Fuchs, I. Petelski, Y. Günzel, M. Salahshour, C.-Y. Lee, J. M. Graving, L. Li, O. Deussen, G. A. Sword, The behavioral mechanisms governing collective motion in swarming locusts. *Science* **387**, 995–1000 (2025).

23. G. Dumas, G. C. de Guzman, E. Tognoli, J. A. S. Kelso, The human dynamic clamp as a paradigm for social interaction. *Proc. Natl. Acad. Sci. U.S.A.* **111**, E3726–E3734 (2014).

24. A. A. Sharp, M. B. Oneil, L. F. Abbott, E. Marder, The dynamic clamp: Artificial conductances in biological neurons. *Trends Neurosci.* **16**, 389–394 (1993).

25. M. J. McHenry, G. V. Lauder, The mechanical scaling of coasting in zebrafish (*Danio rerio*). *J. Exp. Biol.* **208**, 2289–2301 (2005).

26. A. Strandburg-Peshkin, D. Papageorgiou, M. C. Crofoot, D. R. Farine, Inferring influence and leadership in moving animal groups. *Philos. Trans. R. Soc. B* **373**, 20170006 (2018).

27. M. Mischiati, H. T. Lin, P. Herold, E. Imler, R. Olberg, A. Leonardo, Internal models direct dragonfly interception steering. *Nature* **517**, 333–338 (2015).

28. M. Karakaya, S. Macrì, M. Porfiri, Behavioral teleporting of individual ethograms onto inanimate robots: Experiments on social interactions in live zebrafish. *iScience* **23**, 101418 (2020).

29. L. Ristroph, A. J. Bergou, G. Ristroph, K. Coumes, G. J. Berman, J. Guckenheimer, Z. J. Wang, I. Cohen, Discovering the flight autostabilizer of fruit flies by inducing aerial stumbles. *Proc. Natl. Acad. Sci. U.S.A.* **107**, 4820–4824 (2010).

30. M. J. McHenry, J. L. Johansen, A. P. Soto, B. A. Free, D. A. Paley, J. C. Liao, The pursuit strategy of predatory bluefish (Pomatomus saltatrix). *Proc. R. Soc. B Biol. Sci.* **286**, 20182934 (2019).

31. A. M. Hein, D. L. Altshuler, D. E. Cade, J. C. Liao, B. T. Martin, G. K. Taylor, An algorithmic approach to natural behavior. *Curr. Biol.* **30**, R663–R675 (2020).

32. M. S. Madhav, N. J. Cowan, The synergy between neuroscience and control theory: The nervous system as inspiration for hard control challenges. *Annu. Rev. Control Robot. Auton. Syst.* **3**, 243–267 (2020).

33. S. C. Whitehead, S. Leone, T. Lindsay, M. R. Meiselman, N. J. Cowan, M. H. Dickinson, N. Yapici, D. L. Stern, T. Shirangi, I. Cohen, Neuromuscular embodiment of feedback control elements in Drosophila flight. *Sci. Adv.* **8**, eabo7461 (2022).

34. P. Ramdya, A. J. Ijspeert, The neuromechanics of animal locomotion: From biology to robotics and back. *Sci. Robot.* **8**, eadg0279 (2023).

35. T. J. Prescott, S. P. Wilson, Understanding brain functional architecture through robotics. *Sci. Robot.* **8**, eadg6014 (2023).

484 36. J. Larsch, H. Baier, Biological motion as an innate perceptual mechanism driving social
485 affiliation. *Curr. Biol.* **28**, 3523–3532.e4 (2018).

486 37. T. Pasternak, M. W. Greenlee, Working memory in primate sensory systems. *Nat. Rev.*
487 *Neurosci.* **6**, 97–107 (2005).

488 38. V. H. Sridhar, L. Li, D. Gorbonos, M. Nagy, B. R. Schell, T. Sorochkin, N. S. Gov, I. D.
489 Couzin, The geometry of decision-making in individuals and collectives. *Proc. Natl. Acad.*
490 *Sci. U.S.A.* **118**, e2102157118 (2021).

491 39. T. Walter, I. D. Couzin, TRex, a fast multi-animal tracking system with markerless identi-
492 fication, and 2D estimation of posture and visual fields. *eLife* **10**, e64000 (2021).

493 40. J. D. Davidson, M. M. G. Sosna, C. R. Twomey, V. H. Sridhar, S. P. Leblanc, I. D. Couzin,
494 Collective detection based on visual information in animal groups. *J. R. Soc. Interface* **18**,
495 20210142 (2021).

496 41. W. Wang, L. A. Mateos, S. Park, P. Leoni, B. Gheneti, F. Duarte, C. Ratti, D. Rus, Design,
497 modeling, and nonlinear model predictive tracking control of a novel autonomous surface
498 vehicle, in *Proceedings of the 2018 IEEE International Conference on Robotics and Au-*
499 *tomation (ICRA)* (IEEE, 2018), pp. 6189–6196.

500 42. W. Giernacki, M. Skwierczynski, W. Witwicki, P. Wronski, P. Kozierski, Crazyflie 2.0
501 quadrotor as a platform for research and education in robotics and control engineering, in
502 *Proceedings of the 22nd International Conference on Methods and Models in Automation*
503 *and Robotics (MMAR)*, Międzyzdroje, Poland, 2017, pp. 37–42.

504 43. K. Ogata, *Modern Control Engineering* (Prentice Hall, Upper Saddle River, NJ, 2010).

505 44. D. Gorbonos, N. S. Gov, I. D. Couzin, Geometrical structure of bifurcations during spatial
506 decision-making. *PRX Life* **2**, 013008 (2024).

507 45. J. Thomas, J. Welde, G. Loianno, K. Daniilidis, V. Kumar, Autonomous flight for detection,
508 localization, and tracking of moving targets with a small quadrotor. *IEEE Robot. Autom.*
509 *Lett.* **2**, 1762–1769 (2017).

510 46. D. Panagou, V. Kumar, Cooperative visibility maintenance for leader–follower formations
511 in obstacle environments. *IEEE Trans. Robot.* **30**, 831–844 (2014).

512 47. J.-M. Mongeau, S. N. Sponberg, J. P. Miller, R. J. Full, Sensory processing within cock-
513 roach antenna enables rapid implementation of feedback control for high-speed running
514 maneuvers. *J. Exp. Biol.* **218**, 2344–2354 (2015).

515 48. D. Natesan, N. Saxena, Ö. Ekeberg, S. P. Sane, Tuneable reflexes control antennal position-
516 ing in flying hawkmoths. *Nat. Commun.* **10**, 5593 (2019).

517 49. C. H. Brighton, A. L. R. Thomas, G. K. Taylor, Terminal attack trajectories of peregrine
518 falcons are described by the proportional navigation guidance law of missiles. *Proc. Natl.*
519 *Acad. Sci. U.S.A.* **114**, 13495–13500 (2017).

520 50. G. Amichay, L. Li, M. Nagy, I. D. Couzin, Revealing the mechanism and function under-
521 lying pairwise temporal coupling in collective motion. *Nat. Commun.* **15**, 4356 (2024).

522 Acknowledgments

523 We thank all members of the Department of Collective Behavior who assisted with the project:
524 Renaud Bastien for discussions at the beginning of the project, Shiyu Zhao for fruitful discus-
525 sions regarding the feedback control, Jacob Davidson for data analysis suggestions, Alejandro

Gonzalez-Garcia for helping conduct experiments on watercraft, and Nikolaus Troje for insightful comments. We thank Andreas Poehlmann, John Stowers, and Max Hofbauer from loopbio GmbH for technical support with the virtual reality systems, the animal care staff at the University of Konstanz, including Alexander Bruttel, Christine Bauer, Jayme Weglarski, and Dominique Leo, for help in taking care and prepare fish for experiments. We thank Mathias Günther, Jan Peters, Siyuan Wang, Guangwei Wang, Kajal Kumari, Iacopo Hachen for help in running robot experiments.

Funding

Deutsche Forschungsgemeinschaft (DFG, German Research Foundation) under Germany's Excellence Strategy–EXC 2117-422037984. To I.D.C.: the Max Planck Society, the European Union's Horizon 2020 Research and Innovation Programme under Marie Skłodowska-Curie Grant 860949, the DFG Gottfried Wilhelm Leibniz Prize 2022 584/22, the Struktur-und Innovationsfonds für die Forschung of the State of Baden-Württemberg, the PathFinder European Innovation Council Work Programme 101098722, and the Office of Naval Research Grant N0001419-1-2556 To M.N.: Hungarian Academy of Sciences Grant 95152 (to the MTA-ELTE "Lendület" Collective Behaviour Research Group) and Eötvös Loránd University To L.L.:Messer Foundation Award and Sino-German grant M-0541 To W.W and D.R.: a grant from the Amsterdam Institute for Advanced Metropolitan Solutions (AMS) in the Netherlands. To W.W.: a startup grant provided by the Department of Mechanical Engineering and the College of Engineering at the University of Wisconsin-Madison, and the Office of the Vice Chancellor for Research and Graduate Education with funding from the Wisconsin Alumni Research Foundation

Author contributions:

L.L., M.N., and I.D.C. conceived the idea and designed the project; L.L. conducted the fishvr experiments and collected data, L.L. and G.A. conducted experiments and collected the 3D tracking and matrix data. L.L. and M.N. analyzed data with contributions from I.D.C. and O.D.; L.L., R.W., and W.W. conducted experiments on robots and collected data with contributions from O.D. and D.R.; L.L., M.N., and I.D.C. wrote the initial draft and all authors contributed to the revision of the text.

Supplementary materials

Supplementary Methods

Figs. S1 to S29

Tables S1

Fig. 1. Schematic of the study of sensory-motor control of schooling behavior. **(A)**, The flow diagram of the sensory-motor control of the social response to neighbors. We reverse engineer the sensory-motor control (SMC) of following behavior to a model, which we term as 'BioPD'. **(B)**, A traditional experiment in which two real fish swim together in one bowl-shaped arena. Note that the lines trailing each fish indicate their movement trajectories, which are shown at a 1:1 scale relative to the dimensions of the bowl. The fish themselves are enlarged by a factor of 3× to ensure better visibility. **(C)**, "The Matrix" system, where each arena contains a single individual, each of which can interact with a realtime volumetric projection of the other. **(D)**, Open-loop experiments with one virtual fish as a leader swimming back-forth at a recorded swimming speed (0.04 m/s in average). **(E)**, Experiments with two virtual fish swimming side-by-side as two leaders to verify the sensory-motor control. **(F)**, Experiments with two real fish interacting within "the Matrix" to verify the sensory-motor control of the following behavior. A virtual fish becomes a follower controlled by the BioPD when the real fish becomes a leader (when the real fish swims in front). Otherwise, the virtual fish copies the position and direction of the real fish in the other arena. **(G)**, Evaluating the performance of the BioPD model by comparing it to a model predictive controller (MPC) in three robotic systems (terrestrial, airborne, and watercraft). **(H, I)**, Evaluating BioPD's scalability across three species in groups up to 1024 individuals and with up to 14 robots.

Fig. 2. Reverse engineering sensory-motor control of fish to a bioinspired proportional-derivative controller, 'BioPD'. **(A)**, The local coordinate system is based on the position and direction of the leader. The real fish's swimming speed is resolved into lateral speed v_x and forward speed v_y. **(B)**, Schematic to show the experimental setup, where a real fish (RF) follows one virtual fish (VF) which is swimming back-and-forth in a straight line. **(C)**, The virtual fish exhibits a realistic burst-and-glide swimming pattern for five different average swimming speeds $\bar{v}_{VF}$ (0.04 to 0.08 m/s with an interval of 0.01 m/s). **(D)**, The higher the average swimming speed of the leader, the greater is the distance maintained by the follower to the leader. **(E-F)**, Lateral (**E**) and forward (**F**) speed control as a function of the position of the follower in the local coordinate of the leader with different average swimming speeds. **(G-H)**, Average lateral (**G**) and forward (**H**) speeds as a function of the follower's position in the x (**G**) and y (**H**)-axis in the local coordinate of the leader. The shaded areas denote the standard deviation after 100 bootstraps. In general, the lateral swimming speed, v_x, is less sensitive to the leader's average swimming speed, as there is no difference in both the density (**E**) and average plots (**G**). However, the forward speed, v_y, shows sensitivity in both the density (**F**) and average plots (**H**). **(I)**, The distribution of the derivative parameter K_d is based on the maximum forward swimming speed at each average swimming speed of the leader. **(J)**, The comparison between the experiments and simulations shows that the model describes the experimental data.

Fig. 3. Evaluating the perceptual information utilized in the regulation of social response to a leader. **(A)**, Virtual fish swims with the same average but different instantaneous speeds: burst-and-glide as the control (i) or constant speed as the treatment (ii). **(B)**, Virtual fish swims with different update frequencies at 100 Hz as the control (i) or at 5 Hz as the selected treatment (ii) while keeping a fixed location between updates. **(C)**, Virtual fish swims with different visibilities (always visible as the control (i), or periodically become invisible (time being visible and invisible are both set to 0.2s) as the treatment (ii)) to decouple the presented position and speed information. **(D)**, is the same as **C**, except the virtual fish jumps to a location further away by increasing its speed during the period of invisibility by a factor of 2 as compared to speed during being visible. Selected swimming performances, including relative position (iii-iv), lateral speed (v-vi), and forward speed (vii-viii), are presented.

Fig. 4. Evaluating the BioPD: simulations, experiments in "the Matrix" system and in two virtual leader scenarios, and using robotics. **(A-B)**, Positions of real fish (RF, **A**) as followers and simulated followers controlled by the BioPD (VF, **B**) relative to a real leading fish (positioned at the origin). **(C–D)**, Real (**C**) / virtual (**D**) follower's positions relative to the virtual (**C**) / real (**D**) leader's position in two arenas in "the Matrix" system. The virtual fish in panel **D** represents an avatar of the real fish from panel **C**, unless the real fish in **D** is swimming in front. In that case, the virtual fish in panel **D** is controlled by BioPD. The virtual fish in panel **C** is always controlled by the real fish from panel **D**. The real fish in panel **C** follows the virtual fish (VF, **C**), which represents the real fish shown in panel **D**. **(E-H)**, Distributions of relative distance in the y- (**E**, **G**) and x- (**F**, **G**) axis of the simulations (**E**, **F**) and experiments (**G**, **H**). Jensen Shannon Divergence, JSD= 0.03, 0.0, 0.08, 0.0 for (**E**-**H**) respectively. **(I)**, The setup for two virtual fish leaders swimming side-by-side at different left-right distances and average swimming speeds. **(J)**, The definition of the coordinate system. Origin is the center of the two virtual fish. Positive y points to the head direction of the virtual fish. **(K)**, The model predicts the relative distance between the real fish and the virtual fish swimming at different average swimming speeds. **(L)**, The model also predicts the bifurcations in the following behavior of the real fish when they follow two virtual leaders. **(M)**, Three robots are controlled by BioPD and model predictive controller (MPC) to follow a leader moving in a sinusoidal wave. **(N)**, A comparison of the control energy of BioPD and MPC.

Fig. 5: Assessing the scalability of BioPD across three fish species (up to 1024 individuals) and robots (up to 14). **(A)**, Distance lag plotted against the leader's average swimming speed. **(B, C)**, Normalised turning speed, $u_x/\bar{u}_{\mathrm{L}}$, and forward speed, $u_y/\bar{u}_{\mathrm{L}}$, mapped to left-right distance, x (BL), and front-back distance, y (BL), respectively. Data spans three species: zebrafish (*Danio rerio*, N=20), Golden Shiner (*Notemigonus crysoleucas*, N=10, 30, 70, 150), and Sunbleak (*Leucaspius delineatus*, N=512, 1024). **(D)**, A group of 14 robots exhibiting sequential circular motion. **(E)**, three robots tracing the intricate "CASCB" logo in sequence. **(F)**, 14 robots sequentially emulating a constant-speed fish trajectory. **(G)**, 14 robots mimicking a burst-and-coast fish trajectory, similar to natural fish movement patterns. Scale bar: 1 meter (applies to **D–G**). **(H-K)**, Boxplots featuring the median, interquartile range (IQR), and potential outliers are applied to illustrate the deviations (Δ) of each robot's trajectory from the desired path for conditions **D**–**G**.

Movie 1: Summary video. A video abstract of the study.

Movie 2: An overview of the experiments with virtual fish interacting with real fish. A variety of experiments using our virtual reality platform for freely swimming zebrafish, including: platform validation in "the Matrix"; one virtual fish with varying average speeds, movement patterns, update rates, and visibilities; a Turing test in "the Matrix", and two virtual fish with different average speeds.

Movie 3: An overview of the experiments with robots controlled by BioPD for different pursuit behaviors. A series of experiments demonstrating the application of BioPD to robotic pursuit behaviors, including drone, terrestrial, and watercraft pursuits of a leader moving along a sinusoidal path; 14 robots engaged in sequential circular pursuit; 3 robots sequentially navigating complex letter-shaped trajectories; and 14 robots simulating real fish movements at both constant and varying speeds.

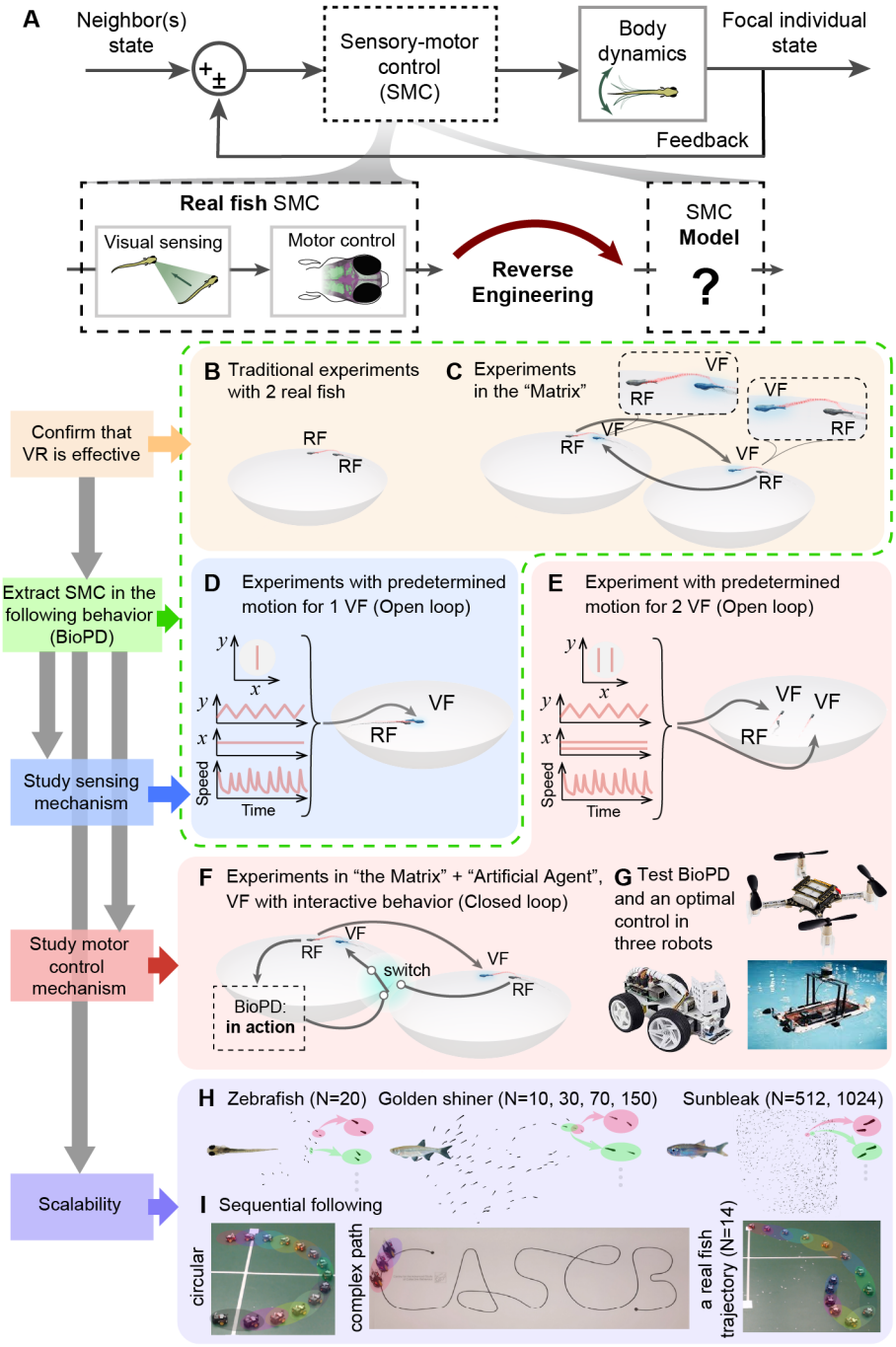
A
Neighbor(s) state
Sensory-motor control (SMC)
Body dynamics
Focal individual state
Feedback
Real fish SMC
Visual sensing
Motor control
Reverse Engineering
SMC Model
?
Confirm that VR is effective
Extract SMC in the following behavior (BioPD)
Study sensing mechanism
Study motor control mechanism
Scalability
B Traditional experiments with 2 real fish
C Experiments in the "Matrix"
D Experiments with predetermined motion for 1 VF (Open loop)
E Experiment with predetermined motion for 2 VF (Open loop)
F Experiments in "the Matrix" + "Artificial Agent", VF with interactive behavior (Closed loop)
BioPD: in action
switch
G Test BioPD and an optimal control in three robots
H Zebrafish (N=20) Golden shiner (N=10, 30, 70, 150) Sunbleak (N=512, 1024)
I Sequential following
circular
complex path
a real fish trajectory (N=14)
VF
RF
Speed
Time

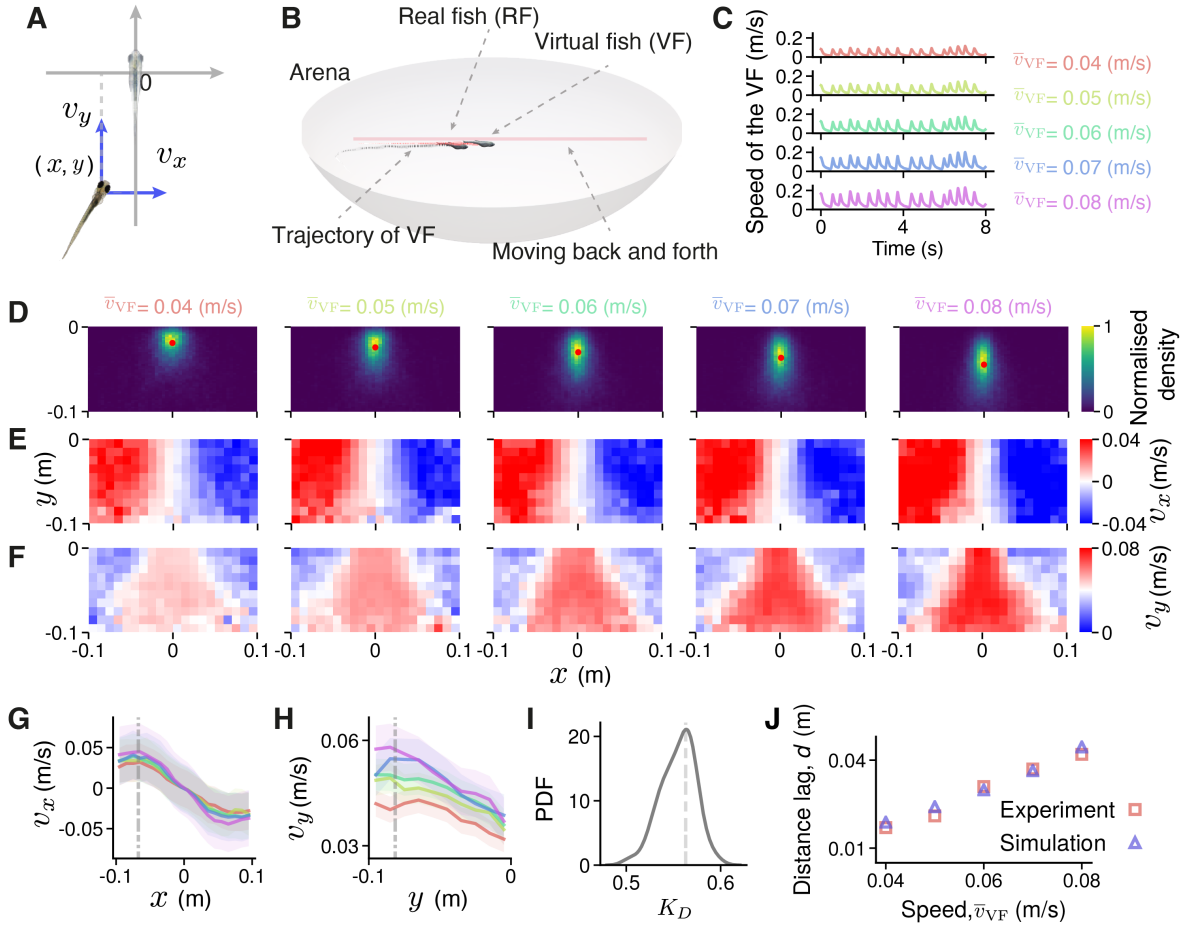

Figure 2: Fig 2

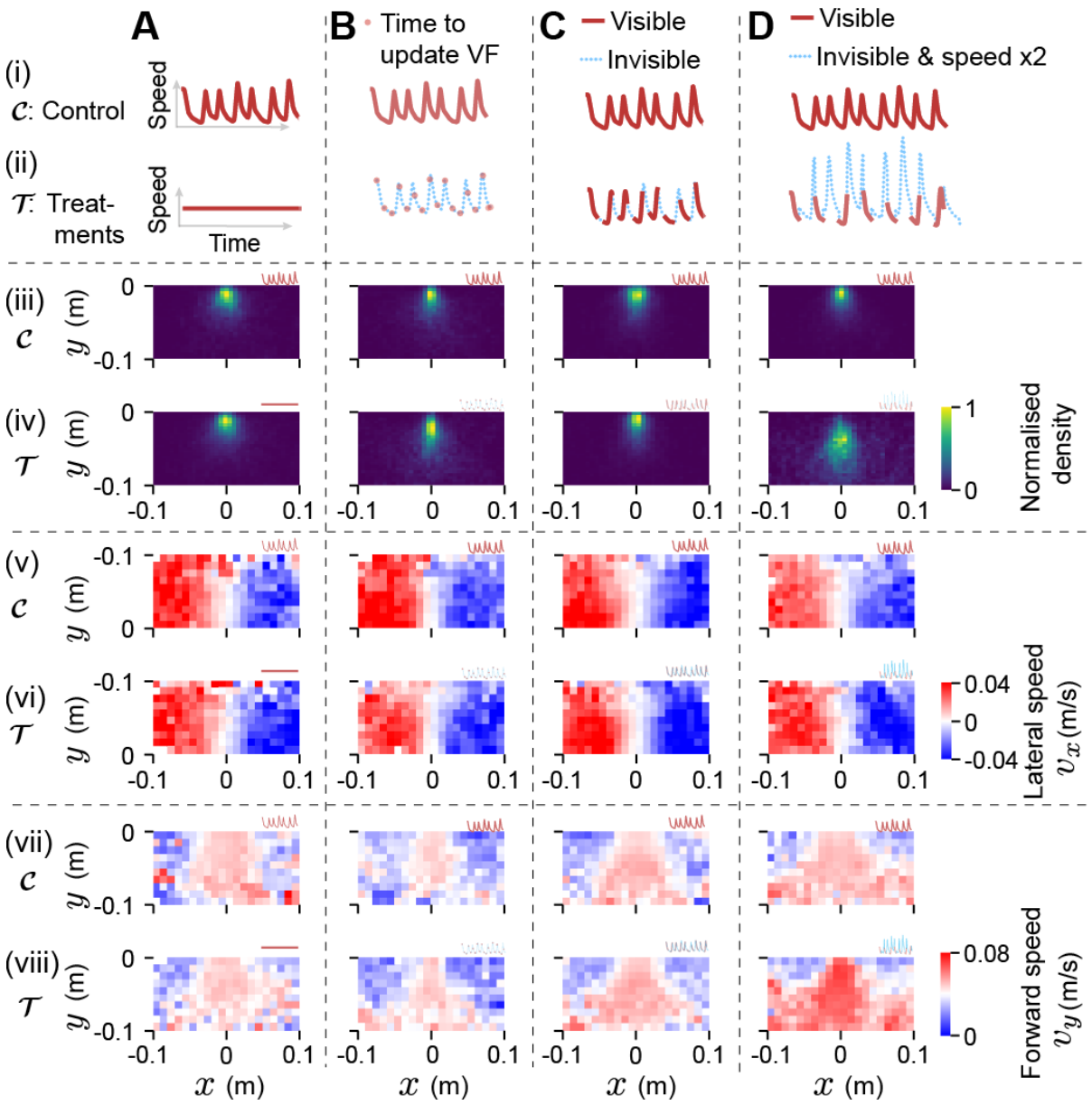

Figure 3: Fig 3

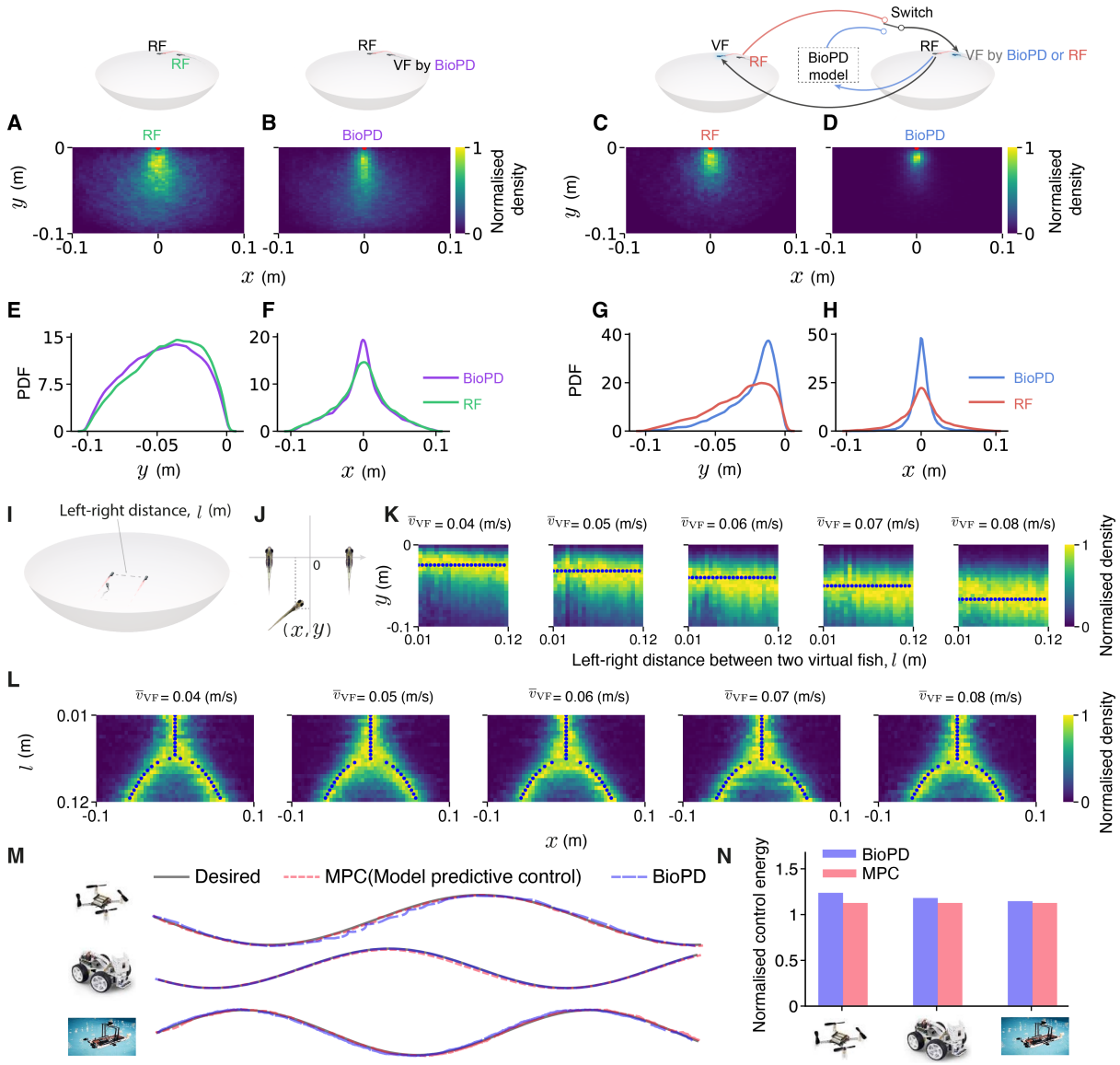

Figure 4: Fig 4

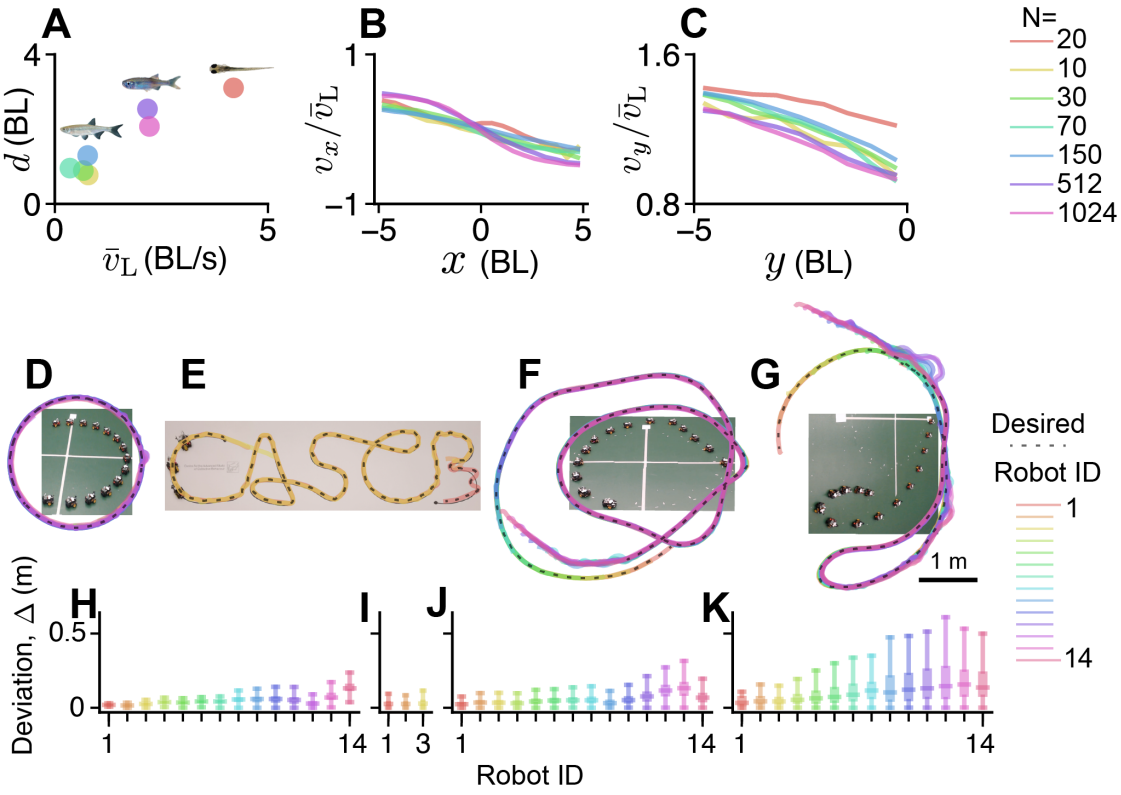

Figure 5: Fig 5

Supplementary Materials for Reverse engineering the control law for schooling in zebrafish using virtual reality

Liang Li[1,2,3,4*], Máté Nagy[1,2,3,5,6*], Guy Amichay[1,2,3,7,8,9], Ruiheng Wu[2,4,1], Wei Wang[10], Oliver Deussen[2,4], Daniela Rus[11], and Iain D. Couzin[1,2,3*]

[1] Department of Collective Behaviour

Max Planck Institute of Animal Behavior, 78464 Konstanz, Germany

[2] Centre for the Advanced Study of Collective Behaviour

University of Konstanz, 78464 Konstanz, Germany

[3] Department of Biology

University of Konstanz, 78464 Konstanz, Germany

[4] Department of Computer and Information Science

University of Konstanz, 78464, Konstanz, Germany

[5] MTA-ELTE "Lendület" Collective Behaviour Research Group

Hungarian Academy of Sciences, 1117 Budapest, Hungary

[6] Department of Biological Physics

Eötvös Loránd University, 1117 Budapest, Hungary

[7] Department of Engineering Sciences and Applied Mathematics

Northwestern University, Evanston, IL 60208, USA

[8] Northwestern Institute on Complex Systems,

Northwestern University, Evanston, IL 60208, USA

[9] National Institute for Theory and Mathematics in Biology,

Northwestern University, Evanston, IL 60208, USA

[10] Department of Mechanical Engineering

University of Wisconsin–Madison, Madison, WI 53706, USA

[11] Computer Science and Artificial Intelligence Lab (CSAIL)

Massachusetts Institute of Technology, Cambridge, MA 02139, USA

*To whom correspondence should be addressed;

E-mail: lli@ab.mpg.de, mate.nagy@ttk.elte.hu, and icouzin@ab.mpg.de.

Supplementary Methods

Experiments with two real fish in the same arena and in the Matrix.

We also conducted 'traditional' experiments (such as those in which real fish swim together) in the same virtual reality arena with the same background projection, but without any virtual fish. This allowed us to analyze data from two real fish swimming in the 3D environment. We calculated and compared the lateral and forward swimming speeds of the following fish to those obtained in the virtual reality system. We next analyzed the lateral and forward speeds of the follower whenever there were leader-follower patterns (see filter and parameters below). Lateral and forward speeds were defined in relation to a coordinate system centered on the leader, with the positive direction pointing towards the leader's head (estimated as swimming direction, Fig. 2A). We averaged the speed over 1 second to obtain the average swimming speed. We divided the speed data into a heatmap with 30 grid cells in the left-right distance and 15 grid cells in the front-back distance. We colored each bin based on the average swimming speed within it.

In our analyses of the leader's swimming properties, we applied an algorithm to identify bursts of high swimming speeds and extract burst-glide swimming periods. Maximum swimming speeds over the extracted burst-glide periods are defined as v_{max}, and the time to reach the maximum swimming speeds is defined as $t_{v_{max}}$ (fig. S7I-K).

Experiments with one virtual fish swimming at different average speeds.

In these experiments, we controlled the virtual fish to swim back-and-forth in the arena at a depth of 0.03 m and along a straight line of length of 0.24 m (Fig. 2B). The average speed of the virtual fish ranges from 0.04 to 0.08 m/s with an interval of 0.01 m/s under

burst-and-glide motion extracted from a random real fish's swimming pattern (average swimming speed is 0.04 m/s and the length of the segment is 8 seconds, Fig. 2C). Faster speeds of the virtual fish are achieved by multiplying the base speed by a factor of (1.25, 1.5, 1.75, and 2). The stable distance lags between the leader, and follower are determined based on the relative position of the follower at a coordinate determined based on the leader (Fig. 2A). The lateral and forward speeds of the follower are calculated as we did for the two real fish case (Fig. 2E, F). Average lateral/forward speed is calculated based on the heatmap along the front-back/left-right direction. The critical turning point of the speed $r_x(r_y)$ is determined based on peak detection. Bootstraps are applied to obtain the statistics of the lateral/forward swimming speeds and the turning points. The parameter K_d is determined by the ratio of the line, which describes the forward swimming speed of the real fish at the critical turning point r_x as a function of the average swimming speed of the leader (see detailed mathematical derivation below). To determine K_p, we simulate (without noise) the follower following a leader swimming at the corresponding average swimming speed. We simulate K_p ranges from 1.2 to 8 with an interval of 0.1. The K_p is optimized to minimize the accumulated differences between the leader-follower distance lags in simulations and experiments.

One virtual fish swimming with different swimming patterns.

In these experiments, we control the virtual fish swimming with different patterns— burst-and-glide and constant speed (Fig. 3A and fig. S11) —but with the same average values (0.04, 0.05, 0.06, 0.07, and 0.08 m/s). The other experimental setting and analyses are the same as described above.

One virtual fish swimming with different refresh frequencies.

In this experiment, we varied the refresh frequency of the virtual fish. The swimming speed was set at 0.04 m/s and the fish was programmed to swim with a burst-and-glide pattern. We set the refresh frequency at 100, 50, 20, 10, 5, or 1 Hz. The refresh frequency determines how frequently we update the virtual fish, which does not affect the average swimming speed. We analyzed the distance lags and lateral/forward swimming speeds in the same way as described above.

One virtual fish with different visibilities

We varied the visibility of the virtual fish by showing it for short periods of time (0.2 s). As a control, we set the virtual fish to be invisible for short periods of time (0.2 s or 0.4 s) and move at the same or double the original speed only when in this invisible state. We set the appearance time to 0.2 seconds to avoid flashing virtual fish. The rest of the experiments and data analyses were the same as described above.

Two real fish in the matrix with BioPD

In these experiments, we controlled the virtual fish in one arena (arena A) based on the behavior of the real fish in the other arena (arena B). While in arena B, we controlled the virtual fish according to the real fish in arena A only when the real fish was swimming behind the virtual fish. Otherwise, the virtual fish was controlled by the BioPD algorithm. We analyzed data from both arenas, as in one arena the real fish followed the virtual fish, and in the other arena, the virtual fish followed the real fish.

Two virtual fish swimming side by side at different average speeds

In these experiments, we controlled two virtual fish swimming side by side and back and forth within the bowl. We varied the left-right distances and average swimming speeds to establish how the real fish controlled its following behavior. The left-right distance was set to 0.01 to 0.12 m in intervals of 0.005 m. The average swimming speed varied from 0.04 to 0.08 m/s in intervals of 0.01 m/s. We analyzed the distance lag of the following real fish in the local coordinate system of the two virtual fish, where the center of the two virtual fish is the origin and the positive y axis is along the virtual fish's heading direction (Fig. 4J). We averaged the distance lag along the left-right distance and plotted it in a heatmap. Similarly, we also averaged the heatmap of the following behavior along the front-back distance to show the decision-making in the x-axis (fig. S17).

Twenty zebrafish experiments

Experiments involved 20 zebrafish that were 24 days post-fertilization, with body lengths ranging from 0.09 to 0.11 m. Videos were captured using a Basler camera at a frame rate of 90 fps. The room temperature was maintained at approximately 26°C. Fish tracking was performed using Trex, which also identified individual fish. We refined the tracking of following behavior based on the following criteria:

First, from the perspective of the leader, the follower must track the leader for a minimum of 1 second. Second, from the perspective of the follower, the leader must be in a leading position for at least 1 second. Third, the angular difference between the two fish should fall within a range of -45 to 45 degrees.

Golden shiner experiments

All data were sourced from the paper and conducted with same filter for zebrafish.

Sunbleak experiments

Experiments were carried out using sunbleak in a large 3 x 3-meter arena. Four Basler cameras recorded synchronously. After video stitching, tracking was conducted using Trex. Outputs from Trex were further refined using the Kalman filter and the Hungarian algorithm. The criteria for filtering following behavior remained consistent with those used for the zebrafish.

Parameter estimation for the model

Our model modifies the traditional PD controller by adding a nonlinear relationship (described by a first-order Gaussian derivative function) between speed and relative position. This function accounts for the phenomenon that when the distance is larger than a threshold distance r_x (r_y), the speed reduces and the follower will reduce its speed to follow the leader. The threshold distance r_x (r_y) corresponds to the peak of the first-order Gaussian derivative function. In other words, the follower should be within the distance threshold to catch up with the leader, and if it is, the performance is similar to the traditional controller. We first theoretically analyze the final stable distance by following derivatives: assume a follower is following a leader on the y-axis; the relative position in the y-axis is Δy. The controller of the follower with a traditional PD controller is:

$$v_{RF} = K_p \cdot \Delta y + K_d \cdot \Delta \dot{y} \tag{1}$$

Then the variation of the distance lag is:

$$\Delta \dot{y} = \dot{y}_{VF} - \dot{y}_{RF} = v_{VF} - v_{RF} \tag{2}$$

Substituting Eq. 1 into Eq. 2 yields:

$$\Delta \dot{y} = v_{VF} - v_{RF} = v_{VF} - K_p \cdot \Delta y - K_d \cdot \Delta \dot{y} \tag{3}$$

Solving this equation, we get:

$$\Delta y = \frac{v_{VF}}{K_p} + \frac{e^{\frac{K_p(C_1-t)}{K_d+1}}}{K_p} \tag{4}$$

Where C_1 is a constant value depending on the initial condition. The final stable distance ($t \to \infty$) will be:

$$\Delta y_{t\to\infty} = \frac{v_{VF}}{K_p} \tag{5}$$

In another way, since $v_{RF} = K_p \cdot \Delta y + K_d \cdot \Delta \dot{y}$ and $\dot{y} = \dot{y}_{RF} - \dot{y}_{VF} = v_{RF} - v_{VF}$, we can rewrite the virtual fish speed as:

$$v_{RF} = K_p \Delta y + K_d (v_{RF} - v_{VF}) \tag{6}$$

Therefore, we get the description of real fish swim speed as:

$$v_{RF} = \frac{K_d}{K_d - 1} v_{VF} + \frac{K_p}{1 - K_d} \Delta y \tag{7}$$

Therefore, we obtained the relationship (first order) between the real fish's swimming speed and the virtual fish's swimming speed. Using bootstrapping, we resampled lateral and forward swimming speeds to get the heatmaps (see Fig. 2E, F in the main text). According to Eq. 7, if Δy is fixed, the relationship between real and virtual fish speeds will be linearly correlated. The ratio is a function of K_d. We then fit the swimming speed of the real fish at the critical distance ($r_x = r_y = 0.07$ m) as a function of the average speed of the virtual fish to obtain the ratio k. Based on the ratio k and Eq. 7, we calculated $K_d = \frac{k}{k-1}$.

The model for two virtual fish as leaders

$$\begin{cases} x_{e1} &= x_F - x_{L1} \\ x_{e2} &= x_F - x_{L2} \\ v_x &= -\left[(K_p x_{e1} + K_d \dot{x}_{e1}) e^{-\frac{x_{e1}^2}{2r_x^2}} + (K_p x_{e2} + K_d \dot{x}_{e2}) e^{-\frac{x_{e2}^2}{2r_x^2}}\right] \\ y_e &= y_F - y_L \\ v_y &= -(K_p y_e + K_d \dot{y}_e) e^{-\frac{y_e^2}{2r_y^2}} \\ r_x &= a \cdot y_e + b \end{cases} \tag{8}$$

where x_{L1} and x_{L2} are the distance differences between the left and right virtual fish and the real fish in a coordinate system determined based on the two virtual fish (Fig. 4J). y_L is the distance difference in the y-axis in the local coordinate system. Because $y_{L1} = y_{L2}$, we set one distance lag y_L for both individuals. Due to the linear perspective, fish perceive the distance in the x-axis to decrease as the distance in the y-axis increases. Parameters a and b are determined based on the fitted critical point in the bifurcation (fig. S17). We fit the bifurcation according to the following steps:

We extract the peaks of the data on the x-axis and then fold the values according to $x = 0$. We then fit a piecewise function to determine the critical point l_c:

$$x_l = \begin{cases} 0 & l \leq l_c \\ \alpha |l - l_c|^\beta & l > l_c \end{cases} \tag{9}$$

where α, β, l_c are fitting parameters, x_l is the detected peak value in the x-axis.

To fit the parameters in the linear perspective model, we first determine the distance lags (d) at different average swimming speeds based on the distributions (fig. S13).

We then fit a piecewise function to determine the critical bifurcation points (l_c). We use these points, along with the distance lag, d, to determine the parameters (a, b) in the linear perspective model.

$$l_c = 0.28d + 0.05 \tag{10}$$

Because the distance lag, d, is linearly correlated to the average swimming speeds of

the leader, v, the relationship between l_c and v is also linear and can be described as:

$$l_c = 0.27v + 0.04 \tag{11}$$

We maintained the value of K_d from the 1 virtual fish case and fit K_p based on the observed distance lag in the experiments, resulting in a value of $K_p = 1.9$.

Apply BioPD in multiple robotic platforms (terrestrial, airborne, and watercraft)

In these experiments, we used BioPD and an optimal controller to control three different types of robots: the Crazyflie drone, the SunFounders Robot PiCar-X, and a robot boat from MIT. We created a virtual leader that moved in a sinusoidal curve for the robots to follow, and we implemented BioPD and a model predictive controller (MPC) based on our previous research. We implemented both BioPD and model predictive controller (MPC) based on our previous study.

In order to implement the BioPD controller for the drone, we provided velocity in the x-and y-axes. We used the same values for the proportional (K_p =2.3) and derivative (K_d =0.563) controls. Since the size of the robot is larger than the size of the real fish (1 cm), we scaled the average swimming speed of the leader by a factor of 2 to increase the safety distance. The turning point of the speed control r_x and r_y was also scaled by a factor of 2. The position of the robot was tracked using a Qualisys motion capture system. With MPC, we designed the state as $\boldsymbol{q} = [\boldsymbol{x}, \boldsymbol{y}]^{\boldsymbol{T}}$, and considered a simple kinematic model:

$$\dot{\boldsymbol{q}} = \boldsymbol{u},$$

where $u = [v_x, v_y]^T$. We apply the controller every sampling instant by solving the following open-loop optimal controller with a finite horizon: $\underset{u(\tau)}{min} = J(q(\tau), u(\tau))$ subject to

$\dot{\mathbf{q}}(\tau) = \mathbf{u}(\tau), \mathbf{q}(\mathbf{0}) = \mathbf{q_0}$, where $\mathbf{u}_\tau \in \mathbf{U}, \forall \tau \in [\mathbf{t}, \mathbf{t}+\mathbf{T}]$. $\mathbf{T}$ is the horizon in the controller, and $J(q(\tau), u(\tau))$ denotes the objective function and is described as:

$$J(q(\tau), u(\tau)) = \int_t^{t+T} F(\mathbf{u}(\tau)) + \mathbf{E}(\mathbf{q}(\mathbf{t}+\mathbf{T})), \tag{12}$$

where F is the cost function regarding the desired performance objective, and E is the terminal cost.

Since the robot car cannot move sideways, we cannot directly apply BioPD to control v_x and v_y. Instead, we convert these two speeds into speed $v = \sqrt{v_x^2 + v_y^2}$ and angular speed $\omega = \dot{\theta}$, where $\theta = \arctan(v_y/v_x)$. The state in the MPC here is $\mathbf{q} = [\mathbf{x}, \mathbf{y}, \theta]^\mathbf{T}$. Control energy is estimated by $\int_0^t \mathbf{u}(\tau)^\mathbf{T}\mathbf{u}(\tau)$.

Implementing BioPD for sequentially following of robotic cars, with up to N=14, across different scenarios

We initially tested with 14 robots executing sequential circular tracking (Fig. 5D, H, fig. S27A, and fig. S28A). The 14 robots were initialized in a circular formation and activated using the BioPD algorithm. The leader robot follows a desired circular path with a constant speed of 0.14 m/s, while the subsequent robots track the closest robot ahead, all under the guidance of BioPD. Initially, BioPD results in an overshoot due to the robots' starting positions and velocities. However, after 25 seconds, the followers' distance lag and average following speeds stabilize.

We also applied sequential tracking along a complex path modeled after the "CASCB" logo using three robots (mainly limited by the cross path for a larger number) at a consistent speed of 0.16 m/s (Fig. 5E, I, fig. S27B, and fig. S28B). Despite the path's complexity leading to some deviations in the tracking behavior, the robots effectively maintained their following pattern.

Finally, BioPD also successfully directs 14 robots to sequentially track complex trajecto-

ries derived from real fish experiments, both at a constant speed of 0.14 m/s (Fig. 5F, J, fig. S27C, and fig. S28C) and varying speeds as performed in real fish systems (Fig. 5G, K, fig. S27D, and fig. S28D).

As robots approach the end of the chain, their angular oscillation increases (see fig. S29), leading to greater deviations (Fig. 5H-K). All experiments took place at the Imaging Hangar of the University of Konstanz. The robots' positions were monitored using the Qualisys motion capture system. BioPD was integrated into the ROS2 (Robot Operating System 2) system for the robots.

The filter for the two real fish swimming in the same arena and the Matrix system.

We apply the following filters to the data analysis in both cases: First, the two fish must swim within a distance of 0.005 to 0.2 meters. Second, their difference in depth (along the z-axis) must be within 0.03 meters. Third, these spatial relationships must be maintained for at least 1 second. Supplementary Fig. S3 shows an example of two fish swimming in a leader–follower configuration.

The filter for the data with one virtual fish swimming in the arena.

In order to analyze the distance lag, lateral speed, and forward speed, we applied filters to the data. The filters used for the distance lag analysis and the speed along the x- and y-axes are slightly different because we are primarily interested in the relative stable following distance lag. We added a swimming direction difference filter to the distance lag analysis and shortened the continuous frames to 30 frames (0.3 seconds), which is a typical burst-gliding swimming period for our fish (fig. S7).

We selected data segments in which two fish swam within 0.2 meters in the x- and y-

axes, and within 0.015 meters in the z-axis. The real fish was positioned behind the virtual fish, which acted as the leader swimming in front. The difference in swimming direction between the leader and the follower was within 30 degrees. The virtual fish remained at the center of the bowl (radius 0.1 meters), and the spatial relationships described above were maintained for at least 0.3 seconds.

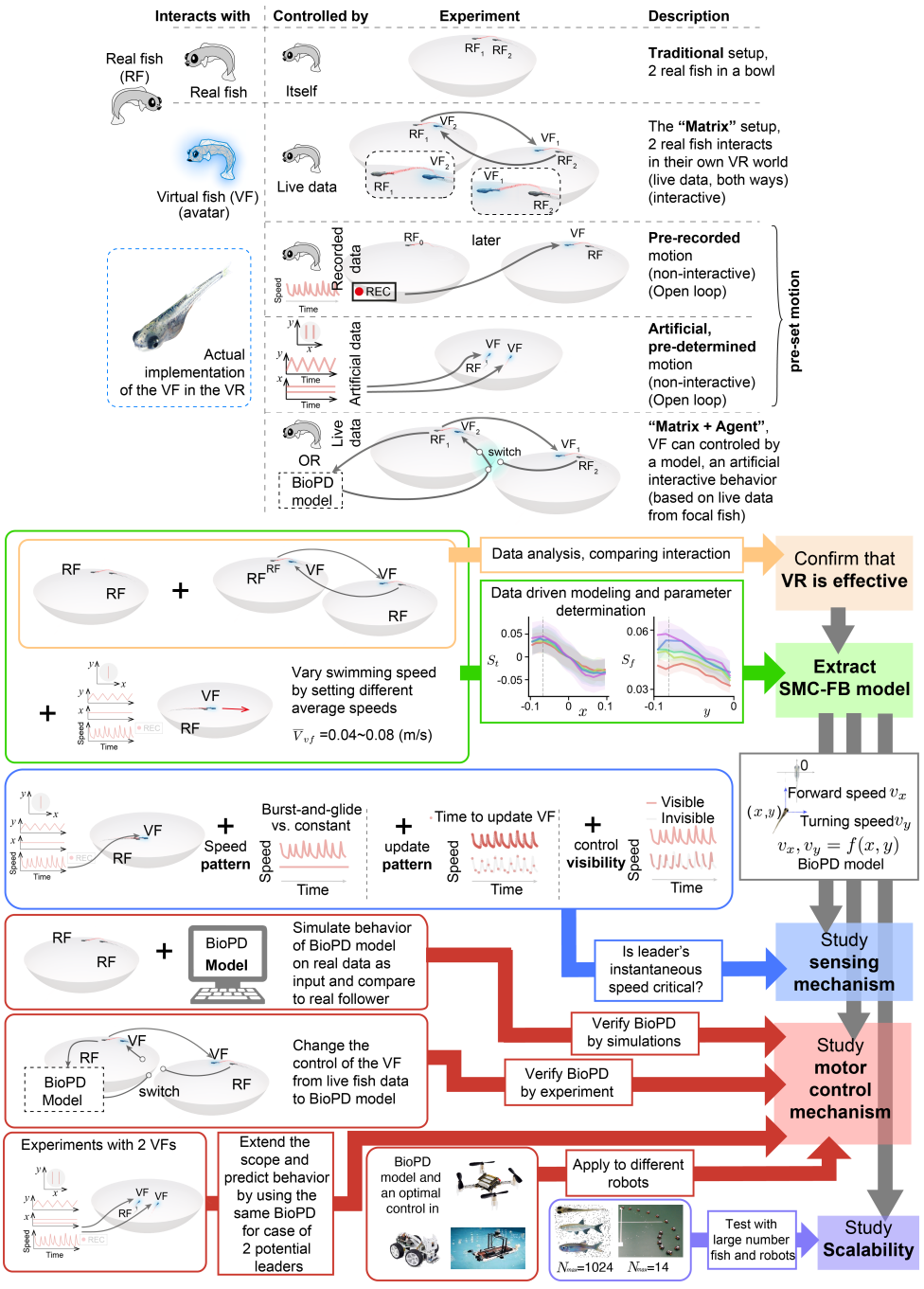

Fig. S 1. Outline of this study. We justify and apply a virtual reality platform to reverse engineer a simple biological-inspired proportional derivate control, which describes sensory-motor control of zebrafish following behavior. With the VR platform, we further checked the model assumption and verified the control. Finally, we applied the BioPD control to three different types of robots.

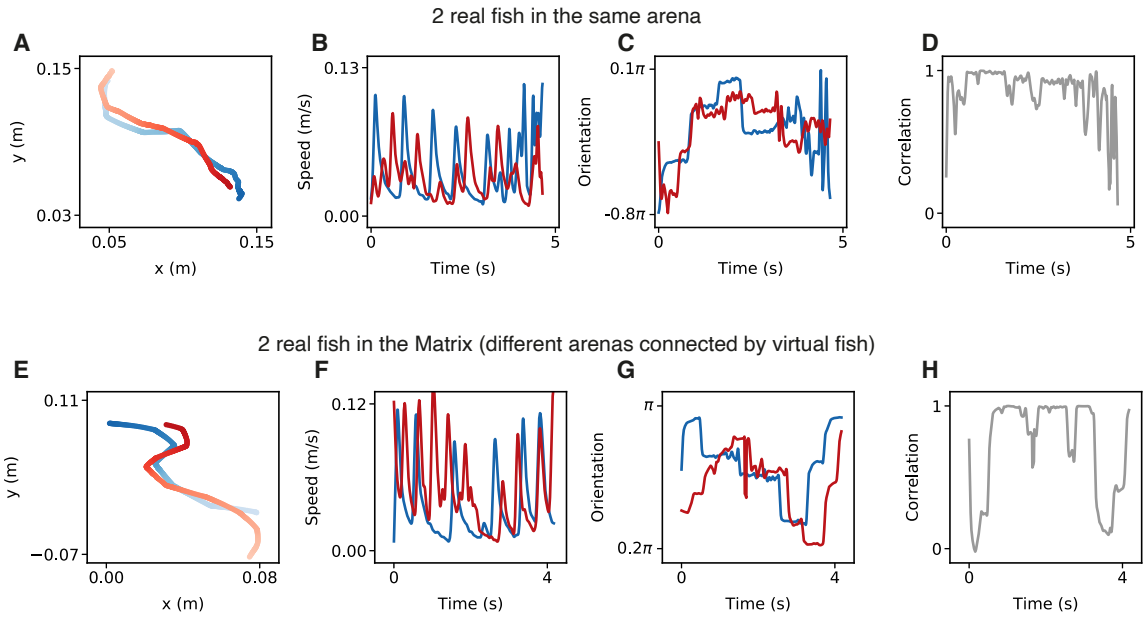

Fig. S 2. Leader-follower swimming trajectories extracted from the experiments in the same arena or "the Matrix" system. Trajectories (**A**, **E**) swimming speed (**B**, **F**) orientation (**C**, **G**) and correlation (**D**, **H**) of two fish swimming in the same arena (**A**-**D**) and "the Matrix" system (**E**-**H**).

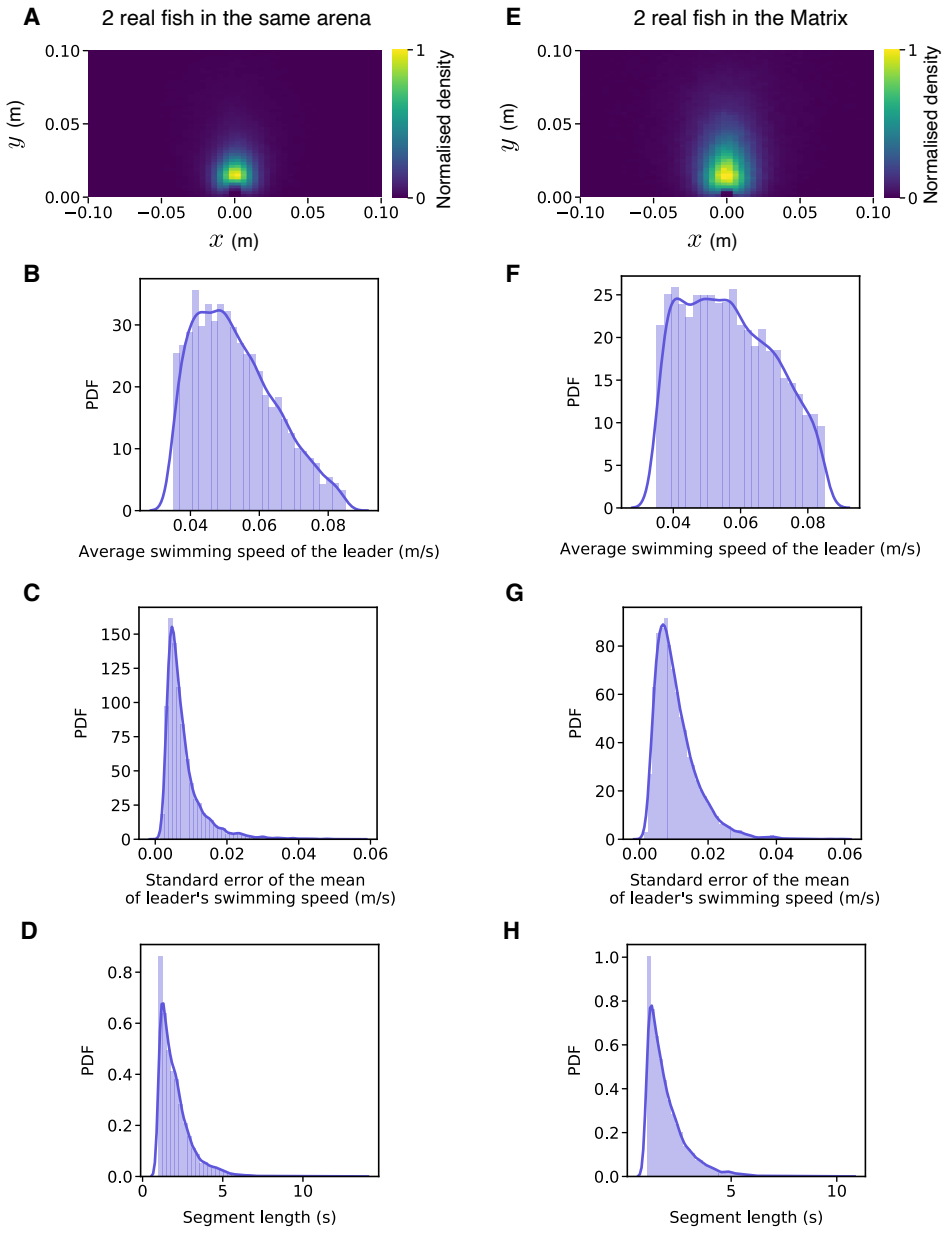

Fig. S 3. Probability density distributions (PDF) of swimming properties of two fish swimming in the same arena or "the Matrix". **A**, **E**, PDF of the leader's position around the focal individual. **B**, **F**, Comparison of leader's swimming speed. **C**, **G**, Comparison of the standard error of the leader's average swimming speed. **D**, **H**, The length of the segments of the pairs.

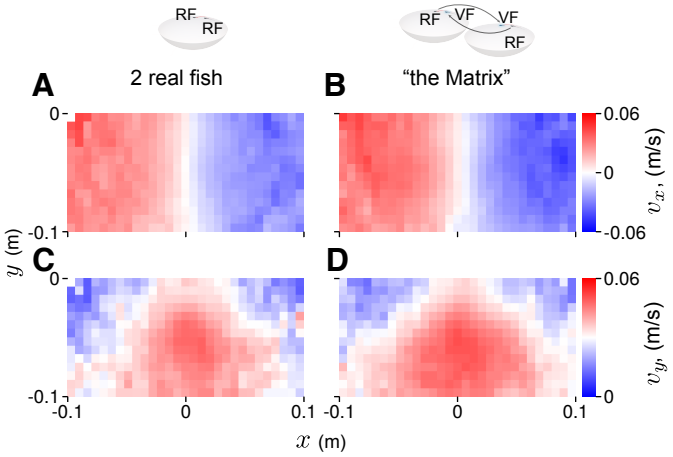

Fig. S 4. The comparisons of the lateral, v_x (A, B) and forward, v_y (C, D) speed as a function of the relative positions of the real or virtual leaders. The relative position of the leader is binned according to the focal individual, and we only consider how the focal fish (the follower) reacts to the neighbor who is swimming in front (the leader).

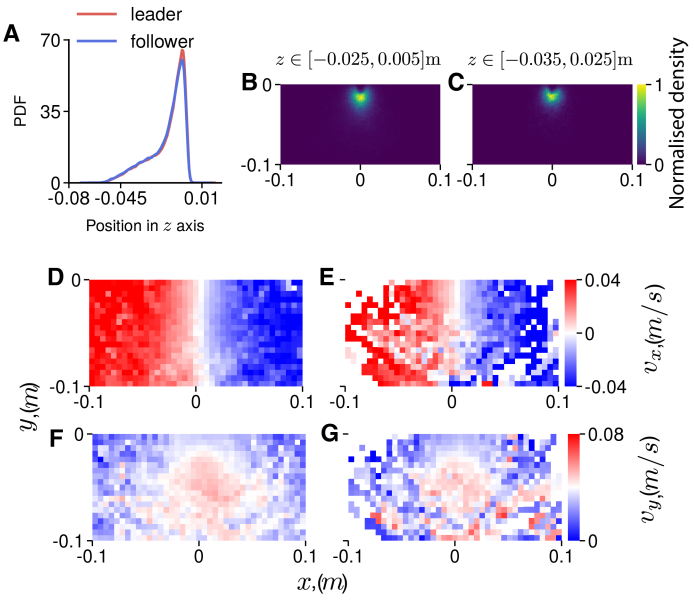

Fig. S 5. Social interaction in the same depth shows similar lateral and forward speeds relative to the leader. **A**, Distributions of two real fish in z axis. **B-C**, Position density of the follower at different ranges of depth. Lateral speed v_x (**D**, **E**), and forward speed v_y (**F**, **G**), as a function of the follower's position relative to the leader at different ranges of depth.

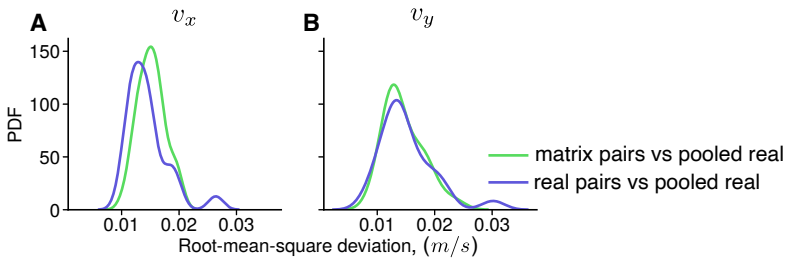

Fig. S 6. Root-mean-square-deviation (RMSD) of the lateral (A) and forward (B) speeds between pairs (real and "the Matrix") and pooled real interaction data. We pooled 22 pairs of real interaction data as a reference and compared the remaining 24 pairs of real interaction data and 24 pairs of virtual (or "Matrix") data to the reference. We found that there was substantial difference between the real and virtual data, as determined by Kolmogorov–Smirnov tests (p=0.26 for lateral speed, p=0.9 for forward speed).

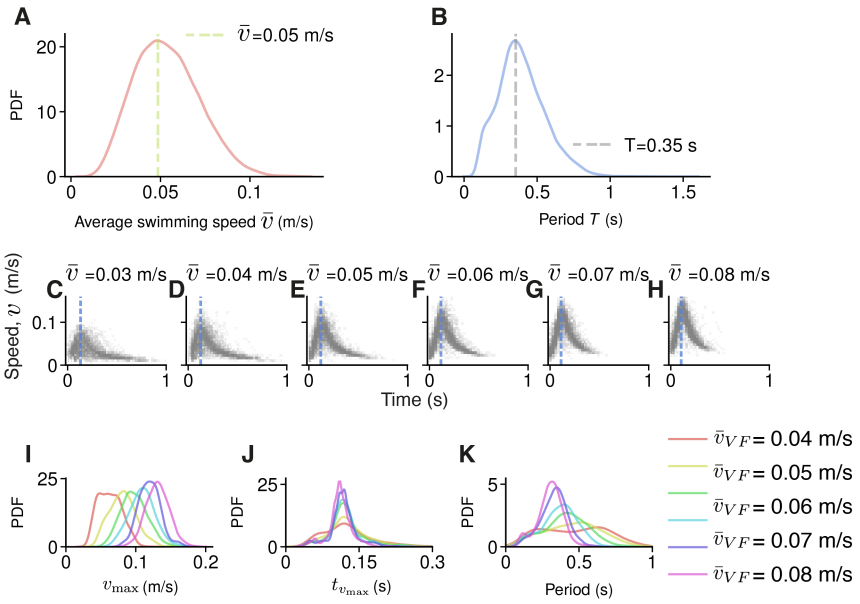

Fig. S 7. Swimming properties of the leader. **A**, Distribution of average swimming speed of the leader over one burst-and-glide period. The typical swimming speed of a leader is around 0.05 m/s. **B**, Distributions of the periods of the burst-and-glide swimming. The typical period is around 0.35 seconds. **C-H**, 500 randomly selected examples of burst-and-glide swimming patterns with varying average speeds. The visual blurriness results from overlapping trajectories, not from a shaded region or error band. **I**, Distributions of the maximum swimming speed under different average swimming speeds. **J**, Distributions of the time when the leader reaches maximum swimming speed. **K**, Distribution of the periods when the leader swims with different average swimming speeds.

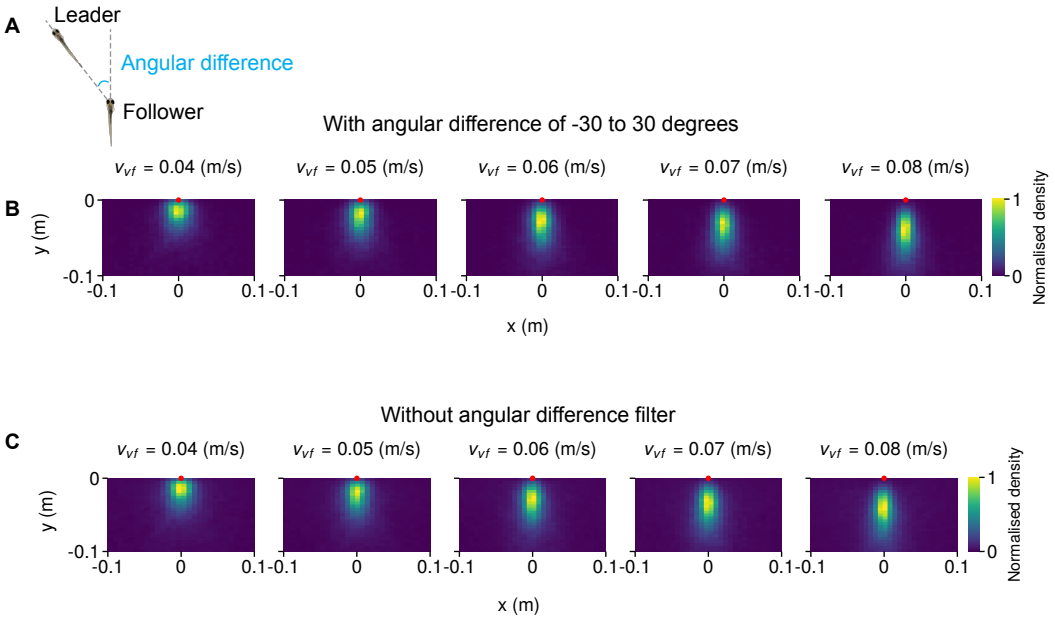

Fig. S 8. A comparison of the position density of the follower relative to the leader's position at different angular differences between the two fish, primarily based on the follower's viewing angle and following behavior. A, Definition of the angular difference. **B**, Follower's position density relative to the leader, positioned at the origin, with an angular difference of -30 to 30 degrees. **C**, Follower's position density relative to the leader at the origin, without considering angular difference.

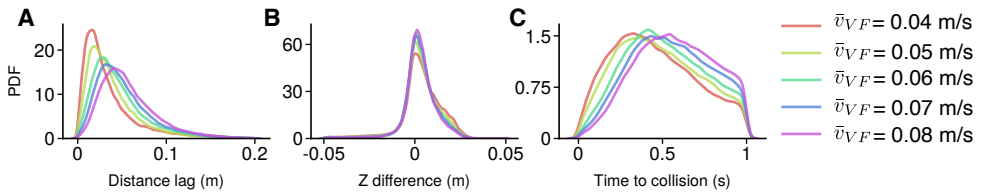

Fig. S 9. A comparison of (A) distance lag, (B) difference in depth in the water column (z axis), and (C) "time to collision" with respect to the current position of the leader (if the leader were to suddenly stop)

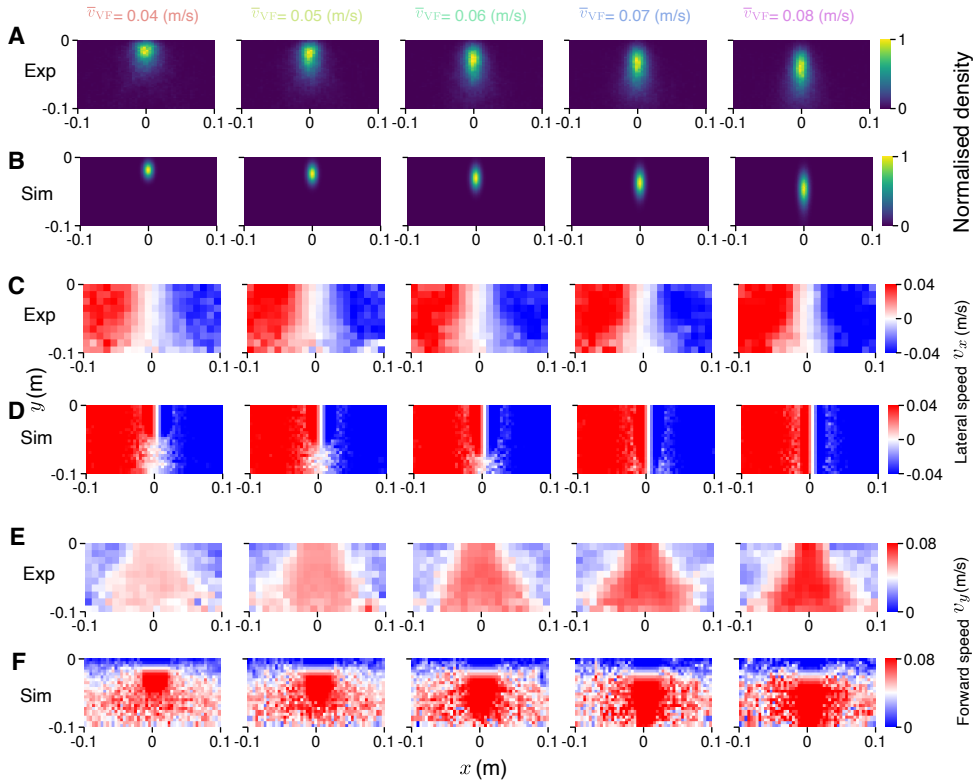

Fig. S 10. Relative position, lateral speed, and forward speed of the follower in experiments (Exp, A, C, E) and simulations (Sim, B, D, F). We initialized the follower's position over a range from -0.05 to 0.05 m on the x-axis and -0.05 to 0 m on the y-axis. White noise was added to the follower's speed control, with a standard variance of 0.016 for the x-axis and 0.45 times the average speed of the follower for the y-axis. The maximum swimming speed was limited to 0.1 m/s. The position density, lateral speed, and forward speed of the follower were then analyzed using the same methods as in the experiments.

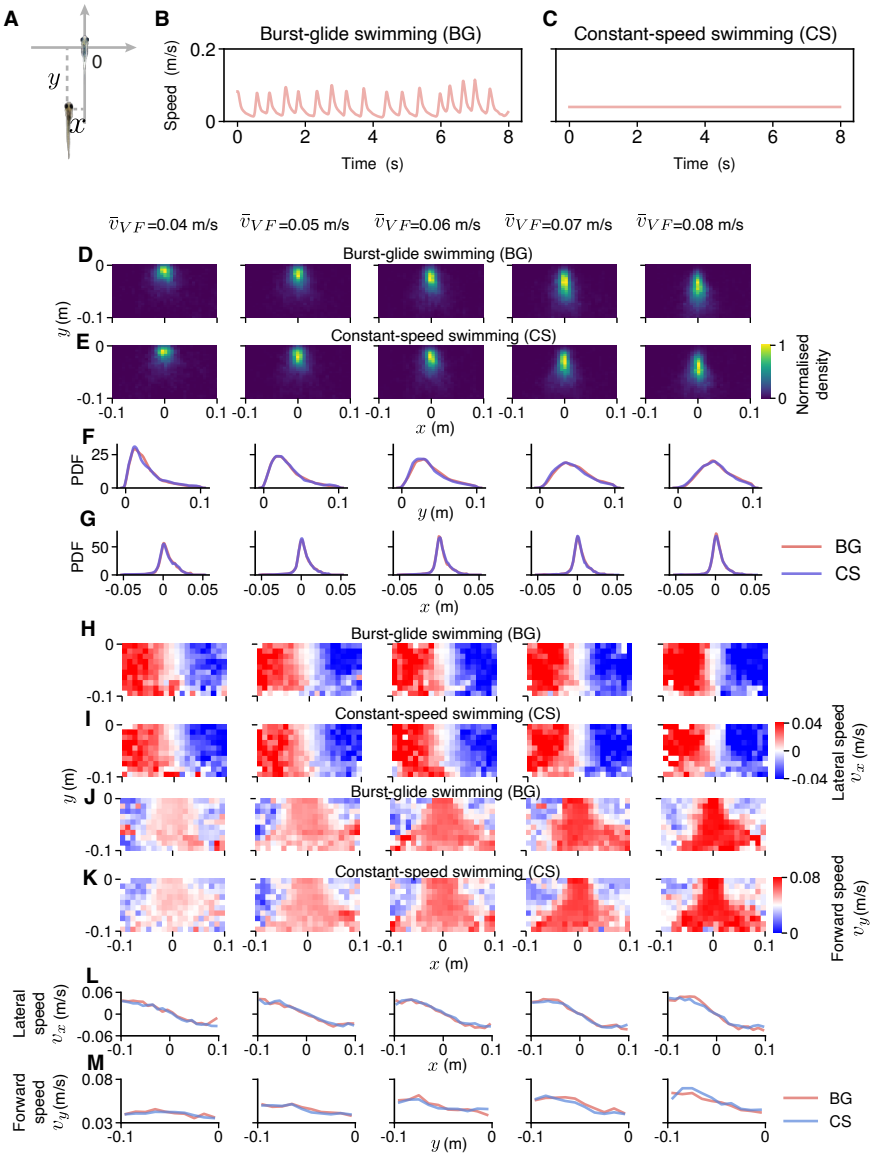

Fig. S 11. Behaviors of the real fish following a leader swimming with burst-and-glide patterns and constant speed patterns. **A**, the coordinate system. **B**, Example of the burst-and-glide (BG) swimming pattern at an average swimming speed of 0.04 m/s. **C** Constant swimming (CS) pattern with an average swimming speed of 0.04 m/s. **D-G**, Positions of the follower relative to the leader swimming with BG (**D**, **F**) or CS (**E**, **G**) patterns. **H-M**, Lateral and forward swimming speed as a function of the neighbor's position with the leader swimming with BG (**H**, **J**, **L**) and CS (**I**, **K**, **M**) patterns.

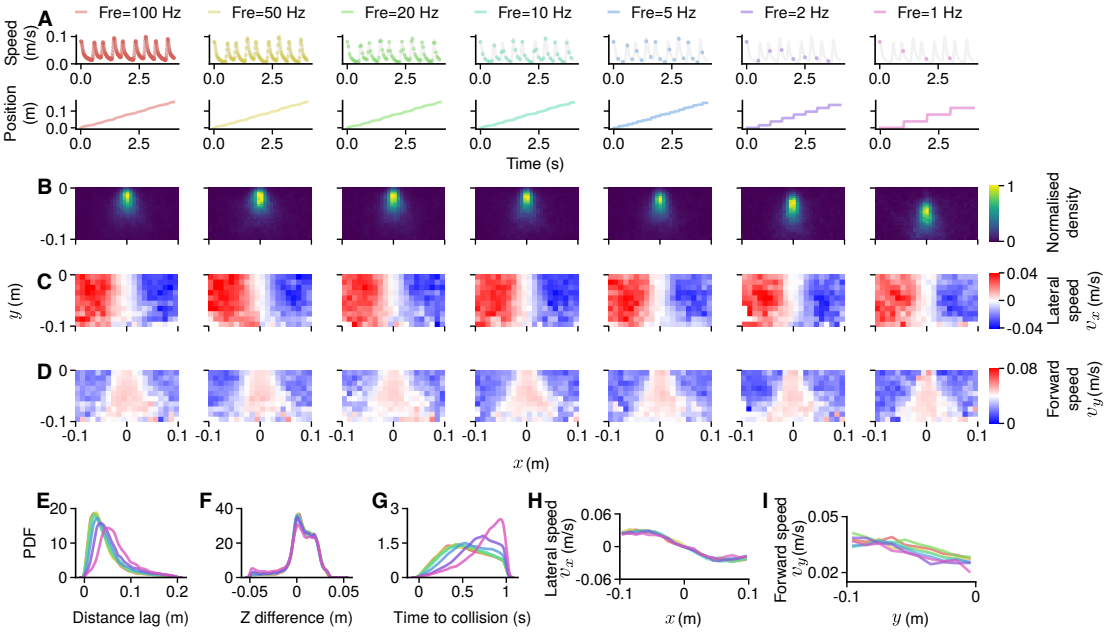

Fig. S 12. Behaviors of the real fish following a leader with different refresh frequencies. **A**, Illustration of the frequency of updating virtual fish swimming as a leader at speed 0.04 m/s and corresponding virtual fish position. **B** Positions of the follower relative to the leader. **C**-**D**, Lateral (**C**) and forward (**D**) swimming speed of the follower as a function of the leader's position. **E**-**F**, Distribution of the distance lag (**E**) and difference in z-plane (**F**) between the leader and the follower. **G**, "Time to collision" for the follower. **H**, Lateral and (**I**) forward swimming speed of the follower as a function of the neighbor's position.

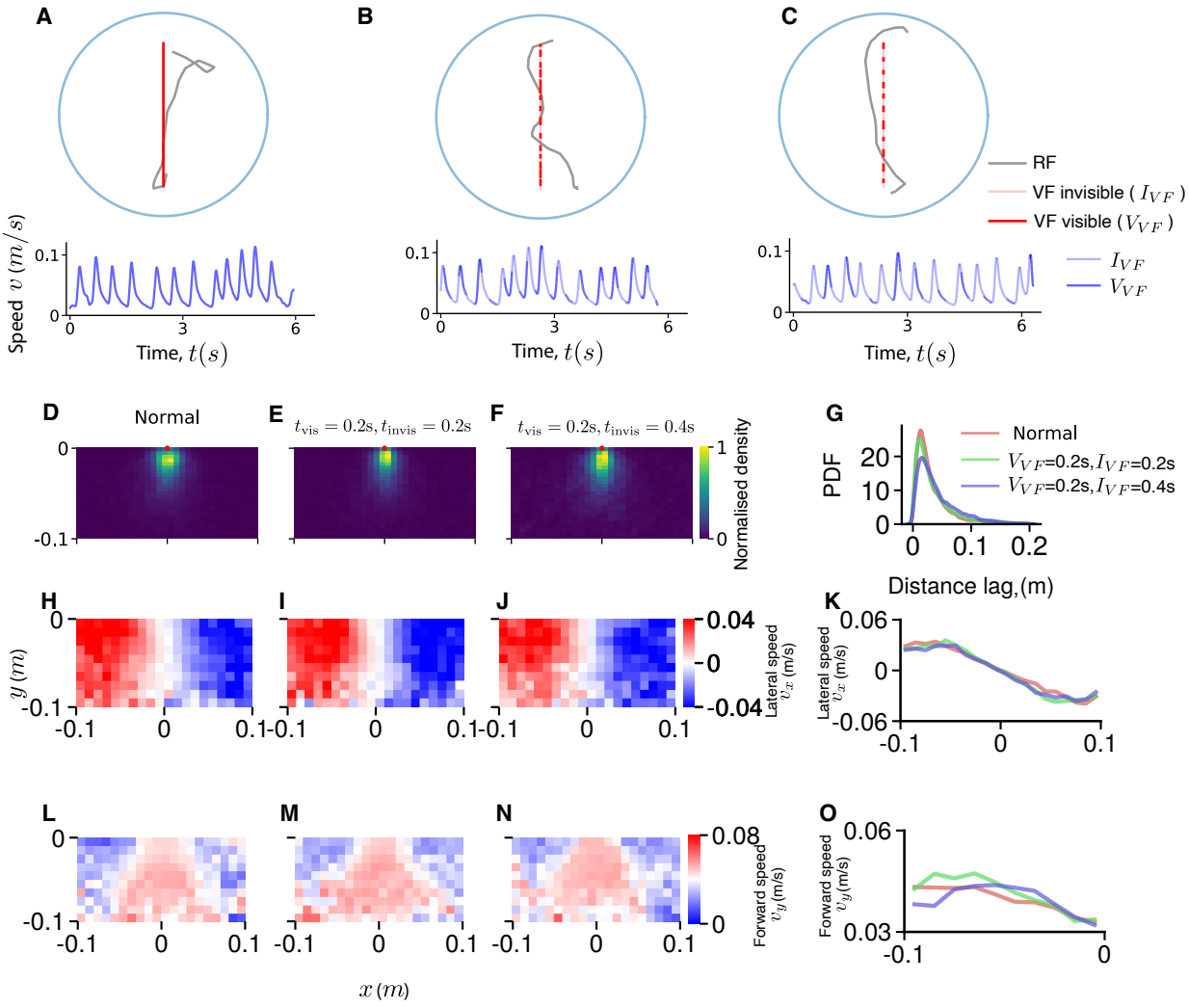

Fig. S 13. Behaviors of the real fish following a leader with varying visibility. **A-C**, Illustration of the visibility control of the virtual fish swimming as a leader at a speed of 0.04 m/s. **D-G**, Positions of the follower relative to the leader. Lateral (**H-K**) and forward (**L-O**) swimming speed of the follower as a function of the leader's position.

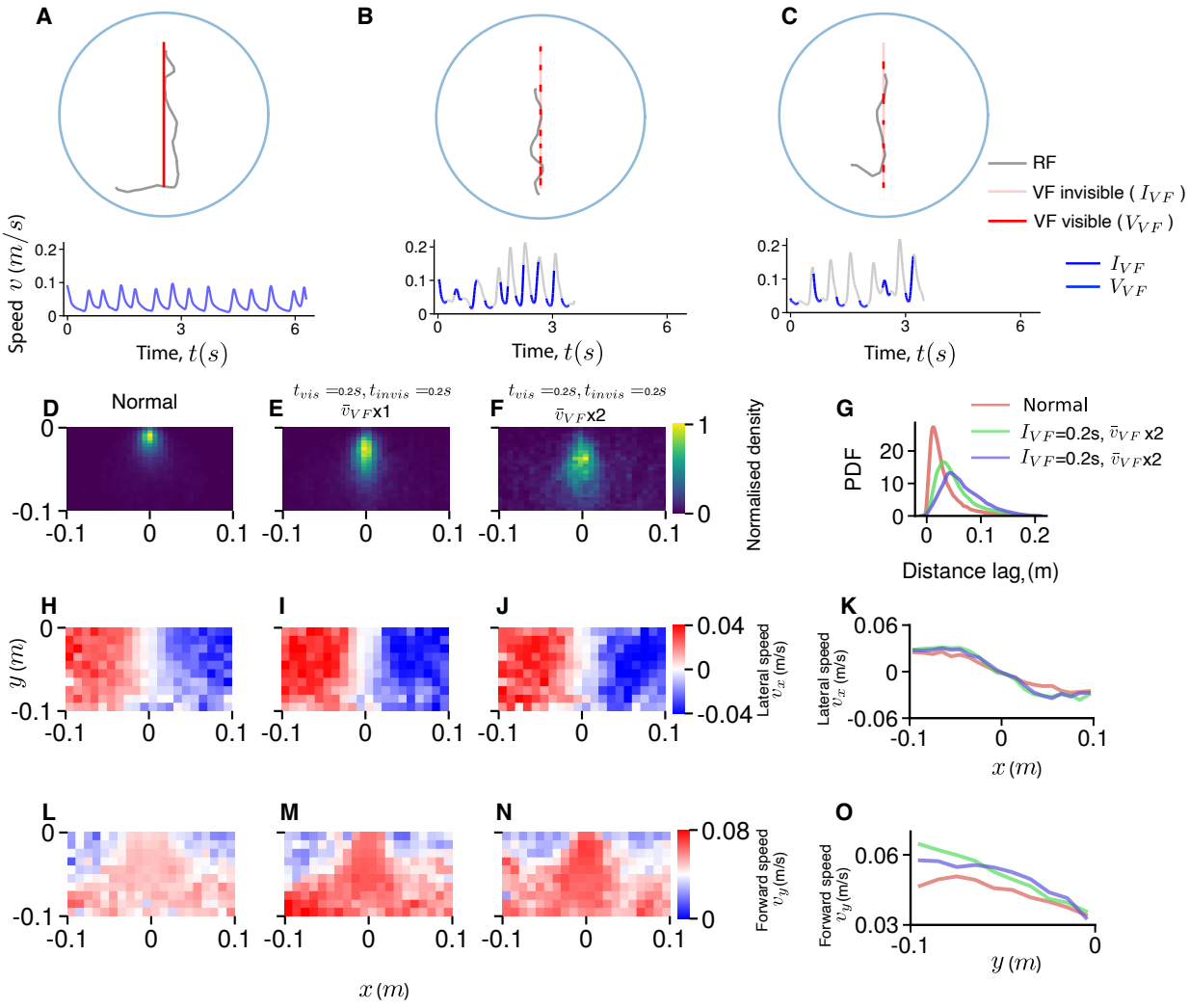

Fig. S 14. Behaviors of the real fish following a leader with varying visibility and speeds of the virtual fish. **A-C**, Illustration of the visibility and speed of the virtual fish swimming as a leader at a speed of 0.04 m/s. **D-G**, Positions of the follower relative to the leader. Lateral (**H-K**) and forward (**L-O**) swimming speed of the follower as a function of the leader's position.

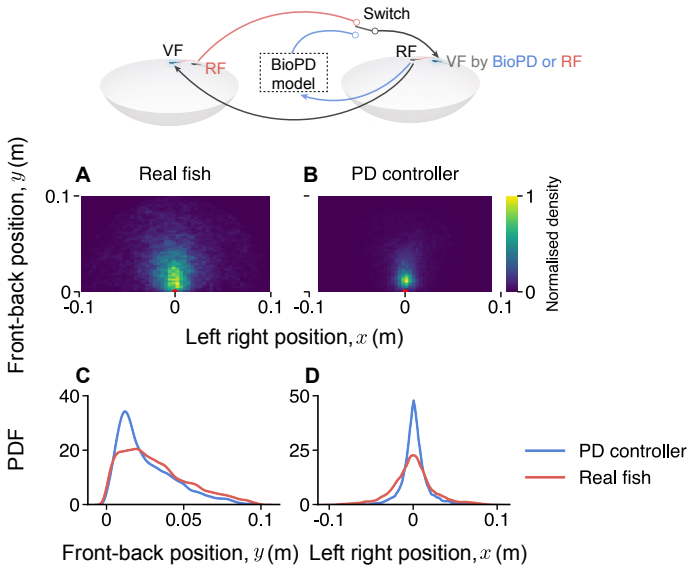

Fig. S 15. Position of the leader relative to the follower in the embodied Turing test. (**A**) The density of the real fish's position (represented by the virtual fish as the avatar) as the leader, relative to the real fish follower at the origin. (**B**) The density of the real fish leader's position relative to the bioPD-controlled virtual fish follower at the origin. (**C**, **D**) A comparison of the front-back and left-right distances between the real follower and the BioPD follower.

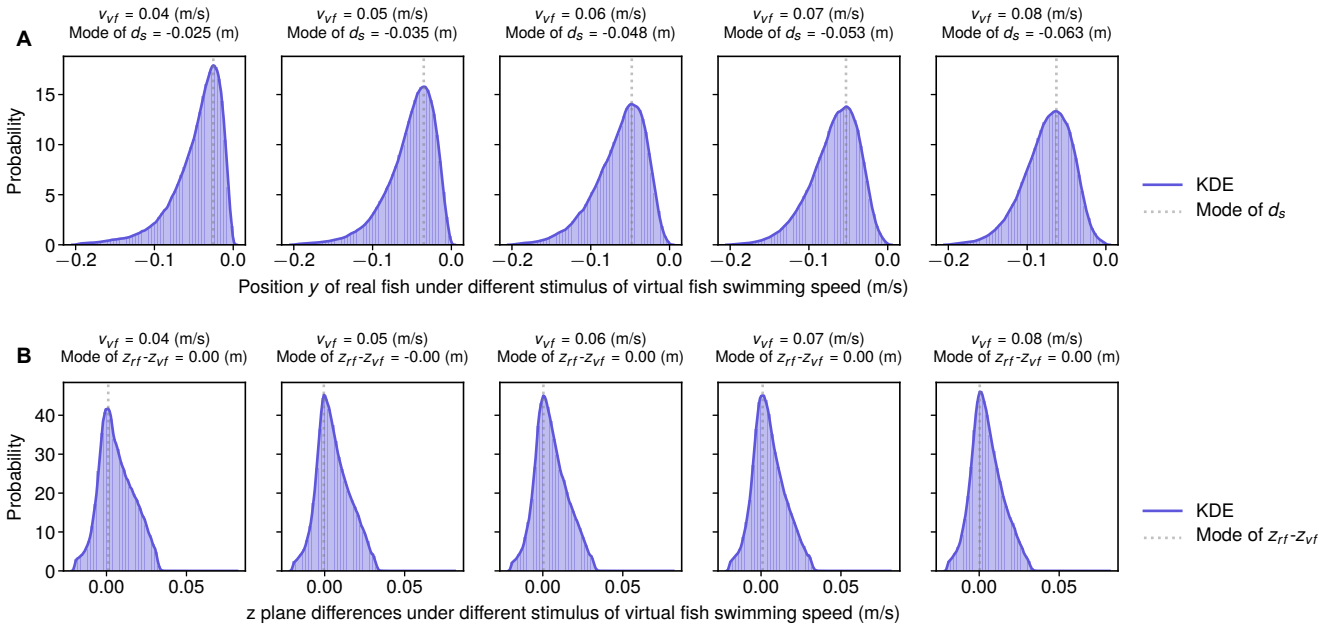

Fig. S 16. Relative position differences between two virtual leaders and one following real fish in y- and z- axis. Distance difference between two virtual fish and real fish in the y-axis (**A**) in the local coordinate based on two virtual fish (origin is the average position of 2 virtual fish and points along the virtual fish head direction) and z-axis (**B**).

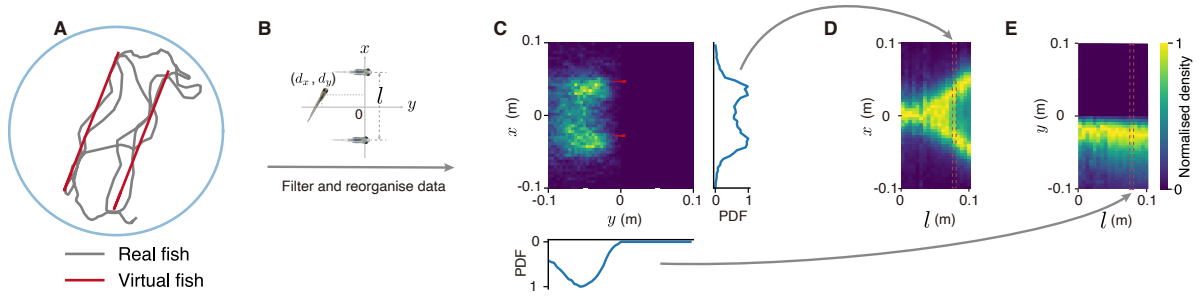

Fig. S 17. Overview of experiments and data analyses with two virtual fish. **A**, Two virtual fish are swimming back and forth in an arena, with an average swimming speed of 0.04 m/s. They are positioned beside each other at a lateral distance of 0.08 m. **B**, The data were organized around a coordinate system with the origin at the centroid of the virtual fish's positions, and decisions were analyzed along the axis perpendicular to their direction of motion. **C**, An example of the real fish's position density in relation to the virtual fish. We calculated the normalized marginal probability distribution of the real fish's position (perpendicular to the virtual fish's movement direction) and stacked these distributions for various lateral distances between the virtual fish. **D**, We are able to maintain the direction of the virtual fish's movement without losing information because the real fish typically maintains a relatively stable front-to-back distance with its virtual conspecifics (**E**).

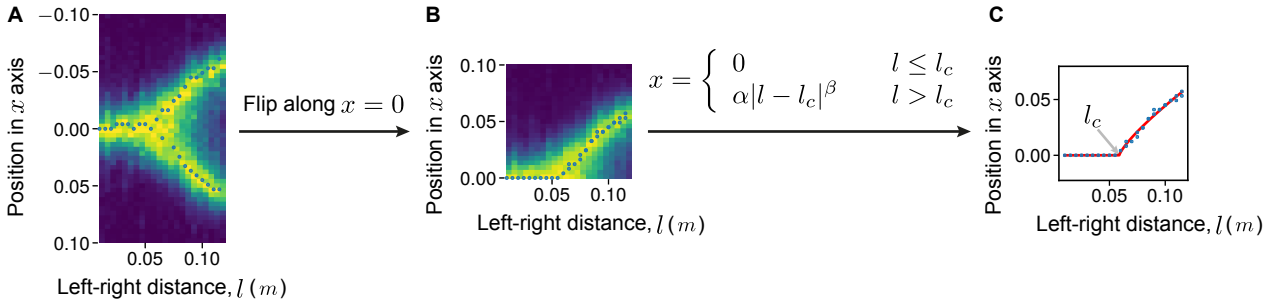

Fig. S 18. Schematic to show how the critical distance l_c is determined based on the heatmap and piecewise function. **A**, Peaks are determined at each left-right distance, l. **B**, We flip the peak values along $x = 0$. **C**, We fit l_c according to the piecewise function.

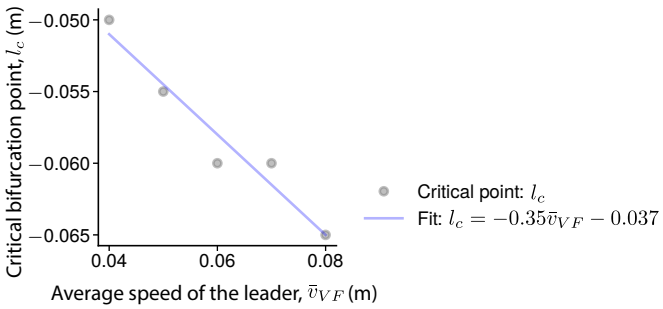

Fig. S 19. The critical bifurcation point as a function of the average swimming speed of the leader.

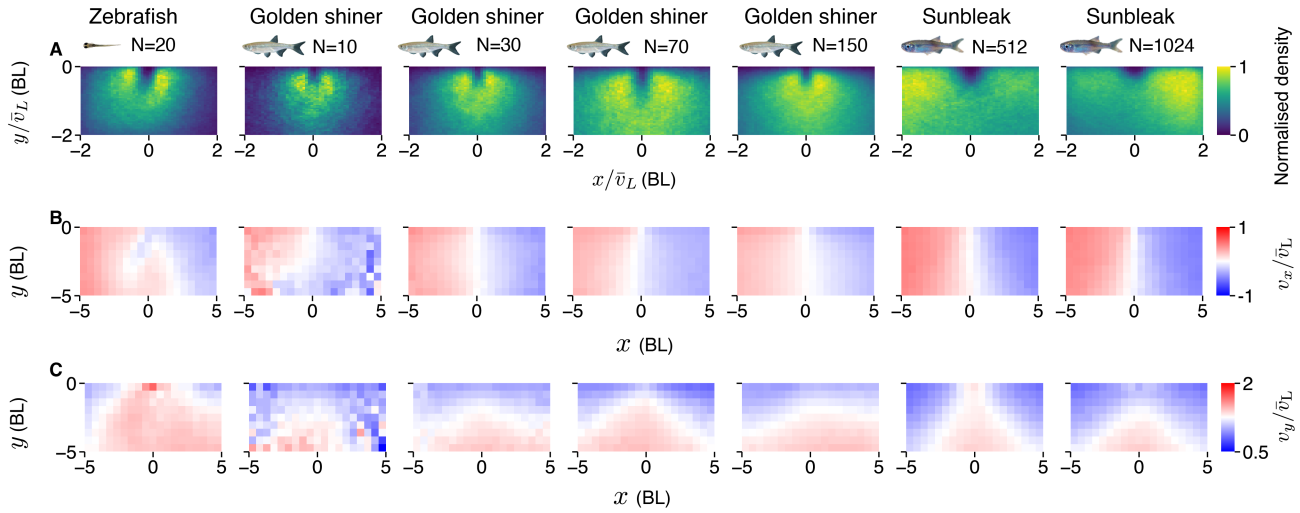

Fig. S 20. Evaluating the scalability of BioPD across three different species up to N=1024. A-C, Normalised position density (**A**), normalised lateral speed ($u_x/\bar{u_L}$, **B**), and forward speed ($u_y/\bar{u_L}$, **C**) of followers in relation to the focal leader positioned at the origin.

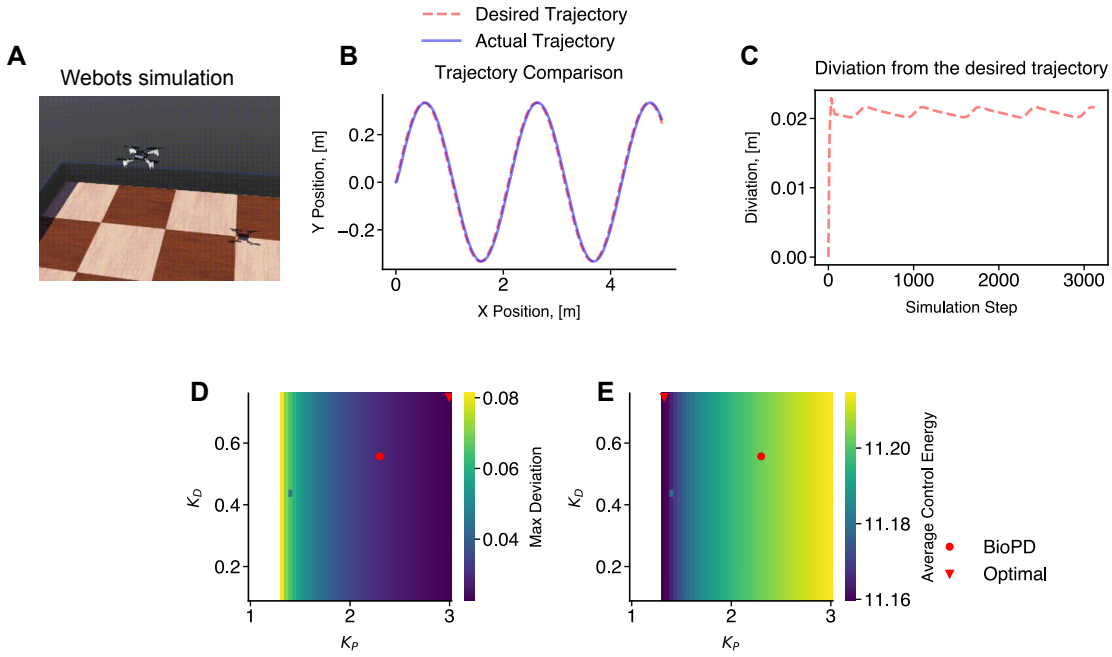

Fig. S 21. Exploration of control parameters with Crazyflie in the Webots simulation environment. **A**, The simulation environment with Crazyflie, controlled by BioPD, with K_P ranging from 1 to 3 in intervals of 0.04, and K_D ranging from 0.1 to 0.75 in intervals of 0.02. **B**, Example of sinusoidal following. **C**, The deviation of the drone under BioPD control from the desired trajectory. **D**, Maximum deviation as a function of proportional and derivative control parameters. **E**, Average control energy as a function of proportional and derivative control parameters. The parameters from the biological system are marked with a red circle, and the triangle marks the optimal parameters for minimal deviation and minimal control energy. As shown, the BioPD parameters strike a balance between deviation and control energy.

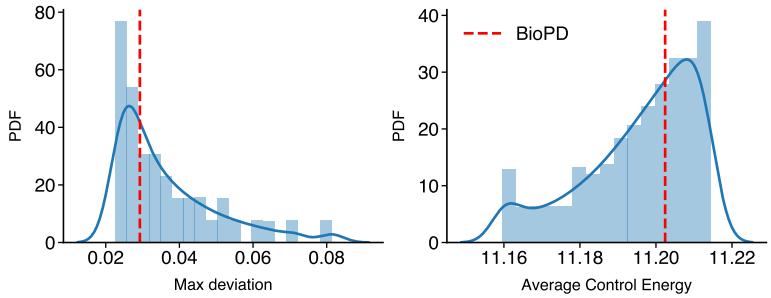

Fig. S 22. Statistical distribution of the maximum deviation (left) and average control energy (right). The red dashed line indicates the biological parameters in BioPD.

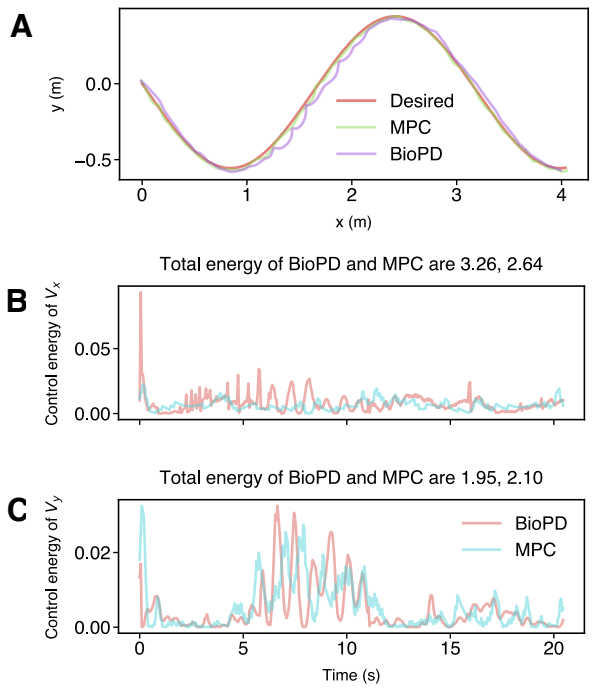

Fig. S 23. Comparison of the performance and control energy of the BioPD and MPC controllers for the Crazyflie drone. **A**, The trajectories of the drone controlled by each method. **B-C**, The control energy of the speed in the x (**B**)- and y (**C**)-axes, respectively.

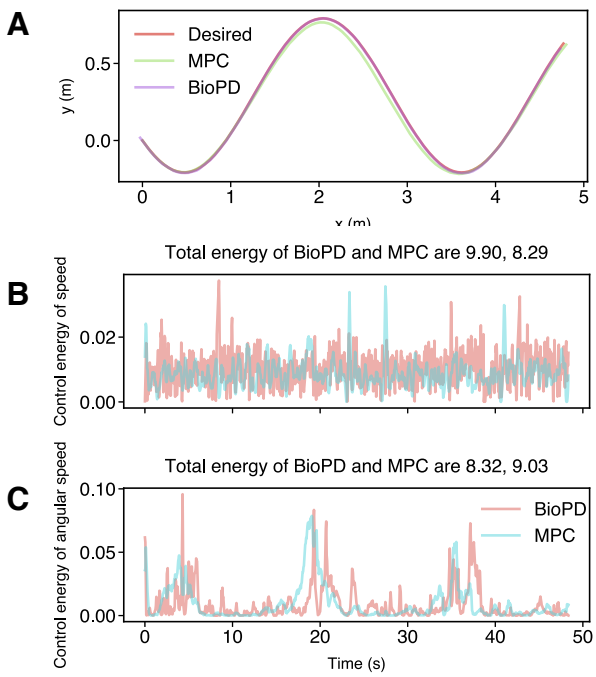

Fig. S 24. Comparison of the performance and control energy of the BioPD and MPC controllers for the PiCar Robot. A, The trajectories of the car controlled by each method. **B-C**, the control energy of the speed (**B**) and angular speed (**C**).

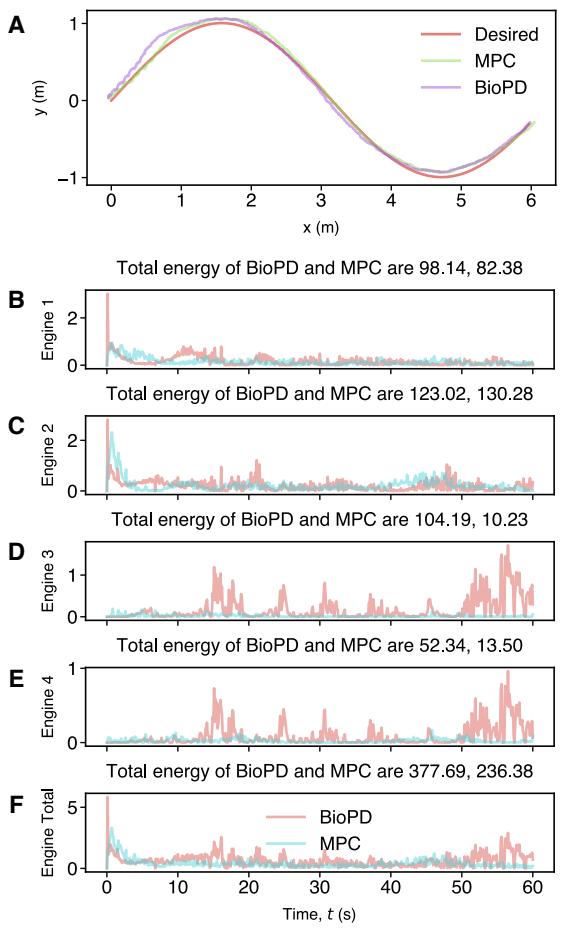

Fig. S 25. Comparison of the performance and control energy of BioPD and MPC controllers for the robot boat. **A**, The trajectories of the boat controlled by each method. **B-E**, The control energy of the four engines within the boat. **F**, Total control energy of the four engines.

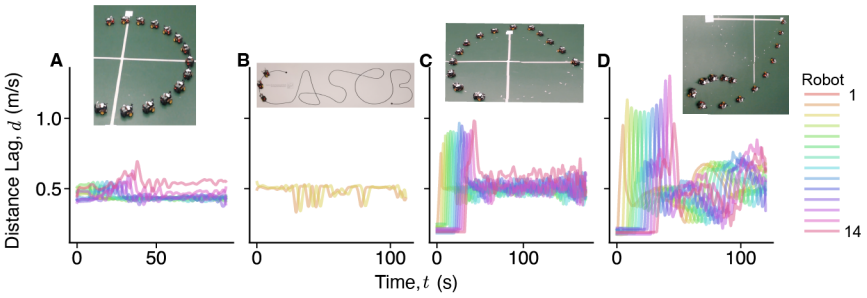

Fig. S 26. The distance lag between successive pairs of robots in the sequence under BioPD control in groups of up to N=14 robots across four scenarios: **A**, 14 robots sequentially following each other in a circle. **B**, 3 robots tracing a complex path modeled after the "CASCB" logo. **C**, 14 robots tracking an actual fish trajectory at a constant speed. **D**, 14 robots mimicking a real fish trajectory, adjusting speeds as the fish did.

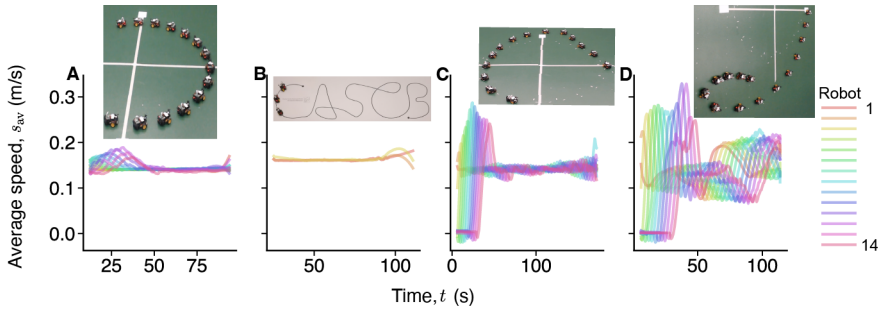

Fig. S 27. Average speeds of followers under BioPD control in groups of up to N=14 robots across four scenarios: A, 14 robots sequentially following each other in a circle. **B**, 3 robots tracing a complex path modeled after the "CASCB" logo. **C**, 14 robots tracking an actual fish trajectory at a constant speed. **D**, 14 robots mimicking a real fish trajectory, adjusting speeds as the fish did.

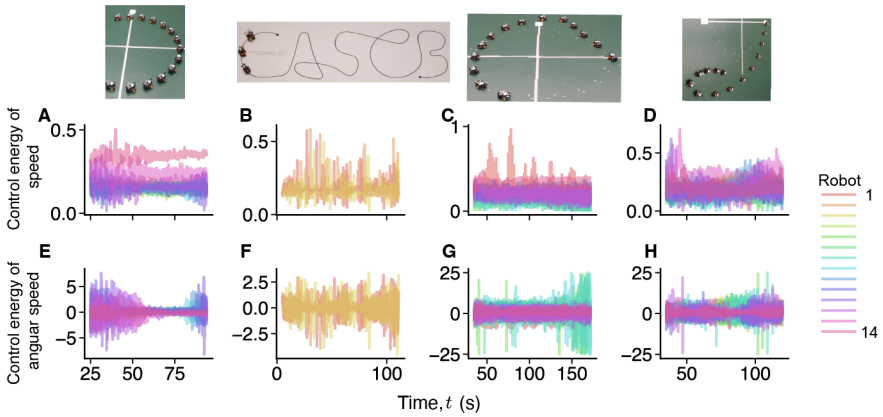

Fig. S 28. Control energy of speeds and angular speeds of followers under BioPD control in groups of up to N=14 robots across four scenarios: A, 14 robots sequentially following each other in a circle. **B**, 3 robots tracing a complex path modeled after the "CASCB" logo. **C**, 14 robots tracking an actual fish trajectory at a constant speed. **D**, 14 robots mimicking a real fish trajectory, adjusting speeds as the fish did.

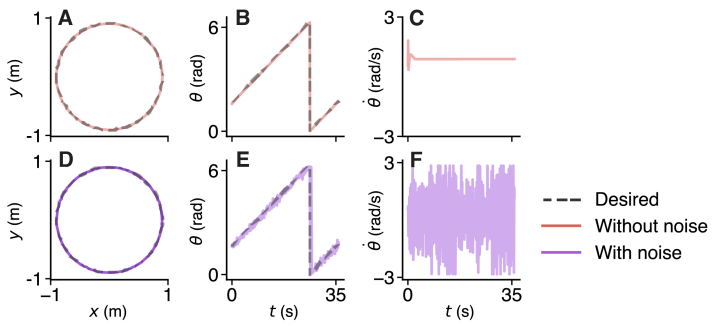

Fig. S 29. Noise induces angular oscillations in BioPD-controlled terrestrial robots. **A-C**, Trajectory, orientation θ, and angular speed $\dot{\theta}$ of the BioPD when terrestrial robots move in a circular path without noise. **D-F**, The same parameters are presented for movement in a circular path with noise.

Trail description	Number of fish	Length of each trail
2 real fish	114 (57 pairs)	40 mins
2 real fish in the Matrix	48 (24 pairs)	60 mins
1 virtual fish at different speeds	39	90 mins
1 virtual fish bout vs constant speeds	22	90 mins
1 virtual fish at different display frequency	25	90 mins
1 virtual fish visibility control	32	90 mins
1 virtual fish in the Matrix to verify model	20 (10 pairs)	90 mins
2 virtual fish at different lateral distances and speeds	198	90 mins

Table S 1. Number of zebrafish for each experiment.